POLITECNICO DI TORINO
Repository ISTITUZIONALE

Validation of High-Fidelity Numerical Simulations of Acoustic Liners Under Grazing Flow

Publisher copyright

(Article begins on next page)

01 September 2025

Validation of High-Fidelity Numerical Simulations of Acoustic Liners Under Grazing Flow

Lucas M. Pereira[*], Lucas A. Bonomo[†], Nicolas T. Quintino[‡], Andrey R. da Silva[§] and Júlio A. Cordioli[¶]
Federal University of Santa Catarina, Florianópolis, 88040-900, Brazil

Francesco Avallone[‖]
Politecnico di Torino, 10129 Torino, Italy

High-fidelity numerical simulations with the lattice-Boltzmann method are carried out to characterize the response of an acoustic liner in the presence and in the absence of grazing flow. The liner's impedance is numerically computed with different methods, i.e. in-situ, mode matching and Prony-like Kumaresan-Tufts, and the results are compared against experimental data, measured in the Federal University of Santa Catarina (UFSC) liner test rig, and the Goodrich semiempirical model. The no-flow results show a reasonable agreement with the semiempirical model but some differences with respect to the experimental educed results are present. It is found that, even in the absence of grazing flow, when applying the in-situ method, there are large variations of the local impedance depending on the sampling location on the face sheet. In presence of grazing flow, simulations with acoustic plane wave propagating in the same direction and in the direction opposite to the mean flow are carried out. Results show that, with the current grid resolution, the numerical educed impedance still overestimates the experimental one particularly at low frequencies, while better agreement is obtained with the in-situ numerical estimation, for both cases. The effects of the grazing flow on the local impedance measurements show high influence of near-orifice wake development. A drastic reduction of the effective percentage of open area is observed when there is grazing flow, as a result of the formation of vortices in the orifices of the liner.

I. Introduction

Acoustic liners are widely adopted technological solution for reducing noise in modern turbofan engines. Typically, liners installed in turbofan engines consist of a rigid back plate, a perforated face sheet and honeycomb cavities, the so-called single degree of freedom (SDOF) liner. The geometric parameters of the liner are specifically designed to attenuate tonal components of the engine fan, which is currently a major noise source in aircrafts [1]. However, as aircraft designs continue to evolve towards greater fuel efficiency, future engines are expected to have different noise characteristics [2]. These changes present significant challenges for noise control, and new solutions such as novel acoustic liner concepts will need to be developed [3]. In order to create effective new solutions, a thorough understanding of the physics behind the typical SDOF liner is critical [4]. Such understanding will provide a solid foundation for the development of innovative noise-reducing concepts.

Liners are passive devices, usually characterized by their acoustic impedance $\tilde{Z}/Z_0 = \theta + \mathrm{i}\chi$, in which θ is the resistance and χ is the reactance. $Z_0 = \rho_0 c_0$ is the characteristic acoustic impedance of air where ρ_0 is the air density and c_0 is the speed of sound. The impedance of a liner depends on its geometry [5], grazing flow velocity [6] and boundary layer parameters [7], temperature [8] and both sound pressure level (SPL) and frequency f of the incident acoustic wave [9].

The influence of grazing flow is of particular interest, and typical experiments are carried out in grazing flow impedance rigs [10–12]. In these facilities, the liner's impedance can be measured using several techniques, such as the

---

[*]MSc Student, Department of Mechanical Engineering, lucas.meirelles@lva.ufsc.br, Non AIAA Member.

[†]PhD Student, Department of Mechanical Engineering, lucas.bonomo@lva.ufsc.br, Non AIAA Member.

[‡]MSc Student, Department of Mechanical Engineering, nicolas.quintino@lva.ufsc.br, Non AIAA Member.

[§]Associate Professor, Department of Mechanical Engineering, andrey.rs@ufsc.br, AIAA Member.

[¶]Associate Professor, Department of Mechanical Engineering, julio.cordioli@ufsc.br, AIAA Member.

[‖]Assistant Professor, Dimeas Department, Corso Duca degli Abruzzi 24, francesco.avallone@polito.it, AIAA Member.

in-situ technique or eduction methods [13–15]. Eduction methods make use of acoustic propagation models and of a proper set of boundary conditions to educe the impedance from the measured acoustic field inside the duct. In the presence of grazing flow, the Ingard-Myers [16, 17] boundary condition (BC) is generally adopted. However, Renou and Aurégan [18] reported a mismatch in the educed impedance when changing the relative direction of propagation of the acoustic wave with respect to the mean flow one, and attributed this mismatch to a failure of the Ingard-Myers BC. Recent works have also shown similar discrepancies in measurements made with the in-situ technique, suggesting a change in the physics, as this technique does not use any information about the flow grazing the acoustic liner [12, 19, 20]. These findings indicate that the physics of the liner in the presence of grazing flow is still not fully understood. Therefore, further investigations are necessary to gain a thorough understanding of the interaction between typical SDOF liners, the acoustic field, and turbulent flow.

High-fidelity numerical simulations offer valuable insights into flow-acoustic interactions and non-linear behavior of acoustic liners. Several studies have used high-fidelity numerical simulations to investigate the effects of grazing flow on flow-acoustic interactions in single cavity resonators [21–23]. These studies achieved good agreement between experimentally and numerically measured impedance. However, since they were limited to single cavity resonators, they did not consider the effects of cavity-cavity interactions, which are present in practical acoustic liners. Moreover, they could not be compared with experimental data obtained with eduction methods. Pereira et al. [24] used a lattice-Boltzmann (LB) very large eddy simulation (VLES) approach to perform scaled-resolved numerical simulations of a realistic multi-cavity liner with and without grazing flow. They also considered different SPLs and acoustic source positions. To validate their numerical results, they compared them with experimental data obtained from the test rig at the Federal University of Santa Catarina (UFSC), finding reasonable agreement for the no-flow cases. However, for the cases with grazing flow, the numerical setup was sensitive enough to capture differences in the measured impedance between upstream and downstream acoustic propagation, but considerably overestimated the resistance. They improved the numerical setup by using a less dissipative solver and better mesh resolution, resulting in better agreement with the reference values. Nevertheless, the effects of the differences between experimental and computational turbulent boundary layer (TBL) parameters remained unclear. This work is a follow-up of the one from Pereira et al. [24], which involved testing a new reference liner geometry in the UFSC test rig under no-flow and maximum Mach number $M = 0.32$ turbulent grazing flow conditions [25]. Tonal acoustic plane waves with frequencies ranging from below to above the liner's resonance at 145 dB are considered, with the acoustic sources at both upstream and downstream positions relative to the sample. The simulations are performed with using an improved version of the LB setup from Pereira et al. [24], and account for a $M = 0.32$ boundary layer profile that matches better the experiments. To improve the analysis of the results, the simulations and the experimental results are compared to a previously validated semiempirical model, which takes into account the influence of the TBL parameters [26]. The simulations' acoustic results are evaluated using three different mesh resolutions and three different approaches to obtain impedance: the in-situ technique, the mode matching method, and the Prony-like Kumaresan-Tufts (KT) algorithm [13, 27, 28]. Additionally, this study analyzes the dependence of the computed impedance on the sampling location when adopting the in-situ technique on the whole face sheet of the liner geometry. The acoustic-induced velocity is obtained in the near-orifice regions by means of the triple decomposition procedure [23], for no-flow and both upstream and downstream sources in the grazing flow cases.

This paper is structured as follows. Section II provides a brief description of the numerical method. We also present the liner geometry, the computational setup and the method used to assess the TBL in both the experiments and simulations. Section III describes the impedance measurement techniques applied to both experimental and numerical results. Section IV presents the acoustic results from the simulations, which are compared to experimental data and to the model's predictions. The experimental and numerical flow profiles are presented and compared, and the effects of the grazing flow and the relative direction of the acoustic source on the liner's impedance are analyzed. Section V provides the main conclusions of the paper.

II. Simulation Procedures

A. Lattice-Boltzmann Method

The lattice-Boltzmann method (LBM) is a numerical approach widely used to address fluid dynamic and aeroacoustic problems [29–31]. Detailed descriptions of the theory involving the LBM can be found in several texts [32–34]. In this work, the simulations are performed with the commercial LBM software *3DS-Simulia PowerFLOW6-2022R1*, using the legacy solver for acoustics [35]. The discrete LBM equations are solved for 19 symmetrical directions in a 3D space (D3Q19). Any solid surface within the lattice is discretized, and the interaction between a fluid particle and

a surface element can be dictated by two boundary conditions: the free-slip and the no-slip. The free-slip boundary condition enforces only zero normal fluid velocity on the surface to which it is applied, while placing no restrictions on the tangential fluid velocity. The no-slip boundary condition enforces both zero normal fluid velocity and zero tangential fluid velocity. A third BC widely used in LBM numerical schemes is the periodic BC, which is usually applied to pairs of opposite limits of the computational domain that are not limited by any surface. In this case, fluid particles leaving the domain on one side will re-enter at the opposite side, instantaneously. This BC conserve mass and momentum at all times [32].

Because of the high Reynolds number for the case of interest, a VLES approach is adopted, where only the large turbulent scales are resolved, while the smaller scales are modeled [36]. The numerical scheme uses a turbulence model that consists of a modification of the two-equation Renormalization Group Theory (RNG) [37, 38], which adjusts the Boltzmann model to the characteristic turbulent time scale. The software applies a wall model based on the law-of-the-wall [38].

B. Liner Geometry and Computational Setup

The SDOF liner sample experimentally tested at the UFSC test rig was 3D printed by stereolithography process. The sample is shown in Fig. 1. It consists of an 8×33 array of square cavities which are $l = 9.906$ mm (0.39 in) wide. The face sheet of the sample is $\tau = 0.635$ mm (0.025 in) thick and has 8 orifices of diameter $d = 0.9906$ mm (0.039 in) per cavity, which gives a single cavity percentage of open area (POA) equal to 6.3%. The total streamwise length of the sample is approximately 420 mm (16.536 in), and its overall POA is 4.2% for the entire surface. The cavities are $h = 38.1$ mm (1.5 in) deep and are completely separated from each other by partition walls $w_p = 2.54$ mm (0.1 in) thick.
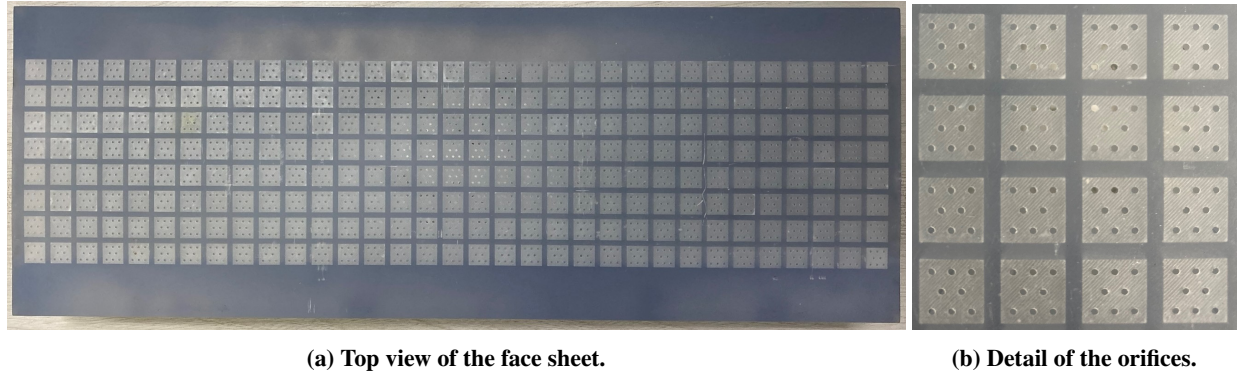

(a) Top view of the face sheet.　　　　**(b) Detail of the orifices.**

Fig. 1　UFSC liner test sample.

The method employed by Schroeder et al. [39] and Pereira et al. [24] for modeling the liner geometry is adopted in this study. The simulations consider a single row of eleven cavities, resulting in a streamwise length of $L = 136.906$ mm (5.39 in), as depicted in Fig. 2.
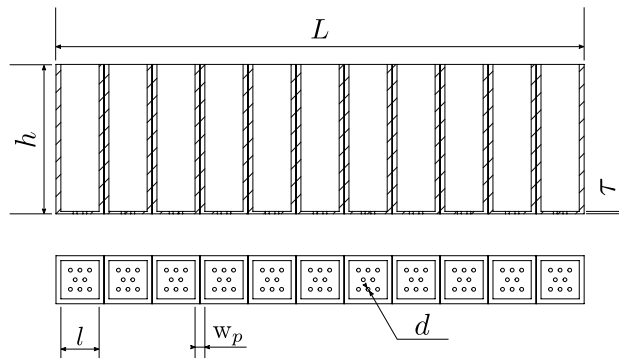

Fig. 2　Modeled liner geometry.

3

The computational domain used in this study is based on the UFSC test rig, as shown in Fig. 3. The coordinate system is placed at the upstream end of the liner sample, where the z axis is defined as $\hat{z} = \hat{x} \times \hat{y}$, although it is omitted in the figure for clarity. The rectangular cross section of the UFSC test rig is $2H$ = 40 mm high (y direction) and $2W$ = 100mm wide (z direction), corresponding to a cutoff frequency for plane wave propagation at 3400Hz [14]. The simulation domain has a width of W_p = 12.446 mm and a height of $2H$ = 40 mm, matching the height of the UFSC test rig. Periodic boundary conditions are applied to the limits of the domain in the z direction.

Fig.3 shows the computational domain used in this study. The orange rectangles represent the channel's inlet and outlet, where a prescribed velocity BC and a static pressure BC are set, respectively. The purple-colored sponge regions are placed at the channel's terminations to prevent reflections of acoustic waves from propagating back towards the sample. The absorbing region is 3λ long, where λ corresponds to the largest wavelength considered in this set of simulations. The gray-colored walls have free-slip BC, and the blue-colored ones have no-slip BC. The boundary layer is triggered by a tripping geometry at a specific position upstream of the liner, as detailed in Fig.3, to match as close as possible the computational boundary layer to the experimental one. The lattice refinement scheme is based on the resolution in the liner's orifices, with coarser grid refinement towards the center and the channel's terminations to reduce the computational cost. In this work, results for resolutions of approximately 10 (coarse), 20 (medium) and 40 (fine) cells per orifice diameter are presented, which were chosen based on previous works involving LBM simulations of acoustic liners [23, 29]. It is worth to mention that, based on previous findings, the grid resolution for which convergence is expected is 60 cells per orifice diameter [23].
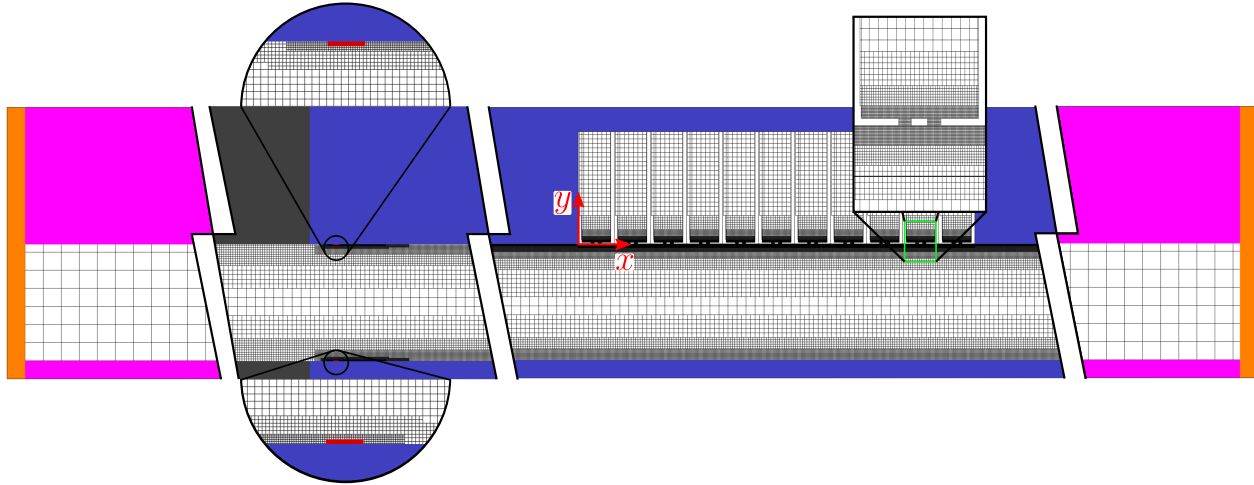
**Fig. 3   Simulation domain: lattice representation and reference coordinate system.**

To perform acoustic simulations, a harmonic acoustic plane wave is superimposed onto the fluid domain, as illustrated in Fig. 4. For this purpose, the *Opty∂B* toolkit is used, as previously done by Avallone and Casalino [23]. For converged simulation results, the channel must be long enough to accommodate at least 10 cycles of the lowest frequency considered. If the simulation includes grazing flow, first a set of simulations are carried out to develop the TBL within the channel. Results from coarser simulations are used to seed higher resolution ones.

## C. Assessment of the Turbulent Boundary Layer

The comparison between the TBLs measured in the experiments and in the simulations is based on the assessment of the x component of the flow velocity U at the upstream end of the liner sample (x = 0 m). The flow velocity is assessed in a set of y positions for a single z coordinate (mid-section of the duct), as shown schematically in Fig. 5.

Experimental flow measurements were obtained using a custom apparatus, which replaced the liner sample with either a Pitot tube or a hot-wire anemometer, as shown in Fig.6. The Pitot tube, which has an external diameter of 3 mm, was unable to acquire near-wall data. However, it provided consistent results and was used as a baseline for comparison with the hot-wire anemometer measurements. In contrast, the hot-wire anemometer was able to measure the TBL in greater detail closer to the wall, and was chosen as the reference for the TBL characterization and comparison with the simulations.

The analytical model presented by Schlichting and Gersten [40] is used for the TBL characterization, through a

(a) Upstream acoustic source.

(b) Downstream acoustic source.
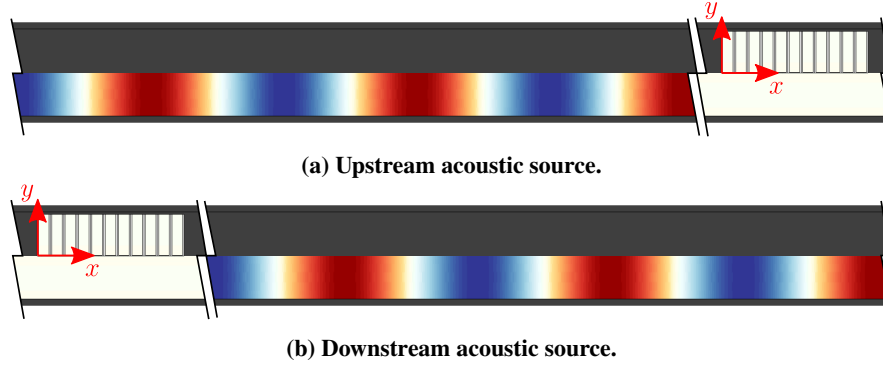
Fig. 4   Acoustic harmonic perturbations superimposed in the computational setup. Red colors denote positive pressure variations and blue colors are for negative pressure variations.
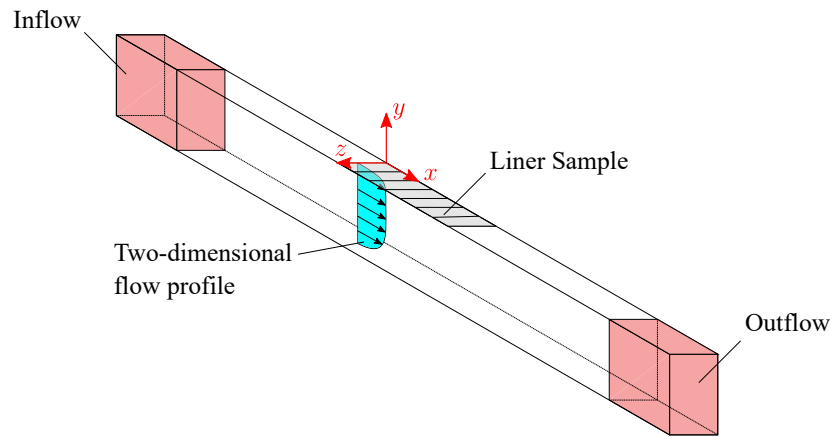
Fig. 5   Schematic representation of the flow velocity assessments.

(a) Pitot tube with 3 mm external diameter.

(b) Hot-wire anemometer.
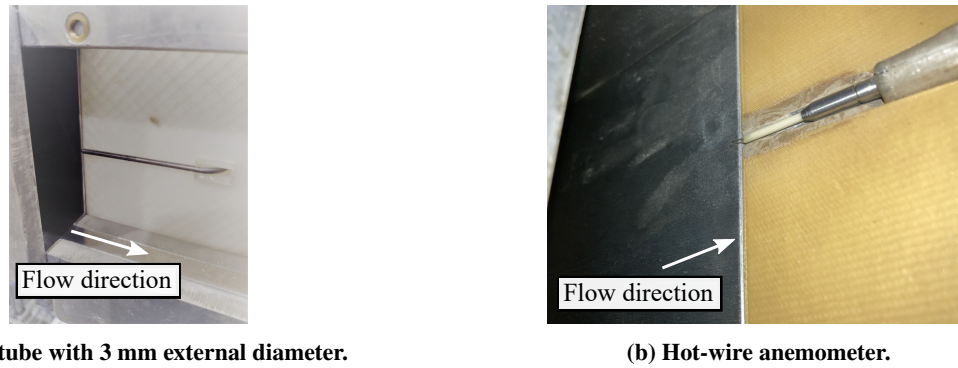
Fig. 6   Experimental assessment of the flow inside the UFSC test rig.

numerical least-square fitting procedure. The flow profile definition relies on the adjustment of two parameters: the friction velocity u_τ and the boundary layer thickness δ. Taking the coordinate system of Fig. 5 as reference, the flow

profile, as per Schlichting and Gersten [40], is defined by:

$$u^+ = y^+, \qquad\qquad y^+ < 5; \qquad (1a)$$

$$u^+ = \frac{\mathcal{K}}{\Lambda} + \frac{1}{4\kappa} \ln\left(1 + \kappa B y^{+4}\right), \qquad\qquad 5 < y^+ < 70; \qquad (1b)$$

$$u^+ = \frac{1}{\kappa} \ln y^+ + C^+, \qquad\qquad y^+ > 70; \qquad (1c)$$

where

$$\mathcal{K} = \frac{1}{3}\left(\ln \frac{\Lambda y^+ + 1}{\sqrt{(\Lambda y^+)^2 - \Lambda y^+ + 1}}\right) + \frac{1}{\sqrt{3}}\left(\tan^{-1}\frac{2\Lambda y^+ - 1}{\sqrt{3}} + \frac{\pi}{6}\right). \qquad (2)$$

The flow variables with the superscript '+' refer to the dimensionless scale of the inner boundary layer. In Eq. 1, $y^+ = |y| u_\tau / \nu$, where ν is the fluid's kinematic viscosity. Similarly, U relates to u^+ by $u^+ = U/u_\tau$. The other parameters are the von Kármán constant $\kappa = 0.41$, $A = 6.1 \times 10^{-4}$, $B = 1.43 \times 10^{-3}$ and $\Lambda = (A + B)^{1/3}$, which gives $C^+ = 5$. These parameters were defined by extensive numerical evaluations and experimental measurements [40].

The determination of δ is challenging and often approximated by δ_{99}, i.e., the y coordinate in which $U(y) \approx 0.99 U_\infty$, being U_∞ the free-stream velocity. However, this is a subjective definition, and any other percentage value can be used. Typically, values between 95% and 99.5% are chosen [41, p. 475]. In contrast, the displacement thickness δ_1 and momentum thickness δ_2 are parameters of the TBL that are not subject to arbitrary choices. The displacement thickness represents the thickness of a zero-velocity layer with the same velocity deficit as the actual boundary layer, while the momentum thickness quantifies the momentum loss in the flow due to the presence of the boundary layer. These two parameters are defined as

$$\delta_1 = \int_0^{-H} \left(1 - \frac{U(y)}{U_\infty}\right) dy, \qquad (3)$$

and

$$\delta_2 = \int_0^{-H} \frac{U(y)}{U_\infty}\left(1 - \frac{U(y)}{U_\infty}\right) dy, \qquad (4)$$

respectively. These parameters are calculated by numerical integration of the measured profiles, both in the experiments and in the simulations.

III. Impedance Measurement Techniques

A. In-Situ Technique

The in-situ technique is a two-microphone method to measure the liner's local impedance [13]. It is based on simultaneous acoustic pressure measurements on both the face sheet $\tilde{p}_f$ and the back plate $\tilde{p}_b$. Fig. 7 presents a schematic, where the two measurement points are shown. The formulation considers that the liner is locally-reactive[*] and that only plane acoustic waves propagate inside the cavity (i.e., the acoustic wavelength is much larger than the cavity's cross section dimensions).

The local liner impedance on the face sheet is determined by

$$\tilde{Z}_f = -i\tilde{H}_{fb}\frac{1}{\sin kh}, \qquad (5)$$

where $i = \sqrt{-1}$, $\tilde{H}_{fb} = \tilde{p}_f / \tilde{p}_b$ is the transfer function between face sheet and back plate measurements and $k = \omega/c_0$ is the free-field wavenumber, with ω being the acoustic wave angular frequency.

Recent studies have shown that as the SPL drops along the sample, due to the liner's attenuation, the local impedance can be different depending on where the pressure acquisition is made [22, 24, 39]. Because of this behavior, the local impedance obtained by a single pair of face sheet and back plate microphones might not be representative for the whole sample. Experimentally, it is not common nor practical to measure the pressure at multiple locations of the sample, due to technical issues, and it is even more difficult to measure at different positions in the same cavity. The experimental

---

[*]In the case of the in-situ technique, the concept of locally-reactive acoustic liner refers specifically to the no energy transmission through the cavity walls condition [13].
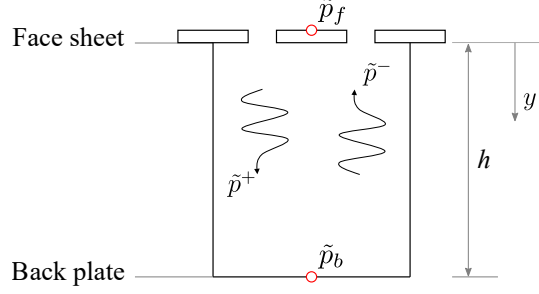
Fig. 7   In-situ technique schematic: pressure probing locations.

results presented in this work were obtained by a single pair of probes located in the third cavity nearest to the acoustic source in the x direction, at a central spanwise position in the z direction. The position of the face sheet probe in the cavity is depicted in Fig. 8a. For further details on the experimental procedures, refer to Bonomo et al. [12]. In contrast, the numerical simulations allow for sampling multiple locations on the face sheet for each cavity. Nonetheless, for better consistency in the comparisons, the in-situ results from the simulations were obtained for a face sheet probe placed in a similar position as in the experiments (as depicted in Fig. 8b), and the back plate probe was positioned at the center of the cavity. This work also presents impedance contour plots calculated with the in-situ technique, which were obtained by sampling the entire face sheet.
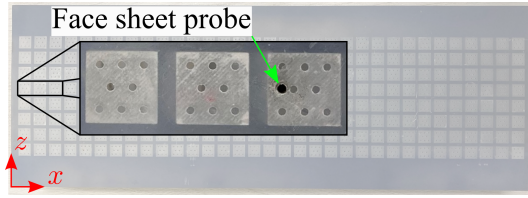
(a) Face sheet probe positioned on the sample for the experiments.
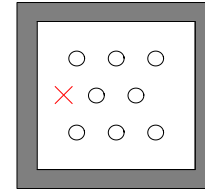
(b) Position of the face sheet probe for the simulations' assessments.

Fig. 8   Position of the face sheet probes for the assessment of the liner's impedance with the in-situ technique.

B. Mode Matching Method

The mode matching (MM) method is an inverse impedance eduction technique used in grazing flow test rigs. It relies on optimization routines to educe the liner's impedance based on the comparison between a theoretical acoustic field and the measured one. The theoretical acoustic field is determined by duct propagation models governed by the convected Helmholtz equation (CHE) [14]. The MM method was initially proposed by Elnady and Bodén [42], and validated later by Elnady et al. [27] and Spillere et al. [43]. In this work a modified version is considered, where only plane waves propagate (also known as straightforward method [44]). Viscothermal energy dissipation is considered through axial wavenumber corrections [45].

For the impedance eduction, two sets of n microphones placed upstream and downstream of the liner at streamwise positions x_i are used to measure the acoustic pressure $\tilde{p}_{\mathrm{exp},i}$. The amplitudes of the acoustic waves $A_j^\pm$ are calculated by an over-determined plane wave decomposition procedure for the $j = 1, 3$ sections of the duct, where $j = 1, 2, 3$ represent the upstream, lined and downstream sections, respectively. In the variables definition, the superscript '+' refers to the downstream direction of propagation of the acoustic wave components, while '-' refers to upstream propagation. A schematic representation of the modal amplitudes in each section j of the duct and the microphones' positions is shown in Fig 9. The plane wave decomposition for the upstream section, for example, is given by

$$\begin{bmatrix} \exp(-\mathrm{i}\zeta_1^+ x_1) & \exp(-\mathrm{i}\zeta_1^- x_1) \\ \exp(-\mathrm{i}\zeta_1^+ x_2) & \exp(-\mathrm{i}\zeta_1^- x_2) \\ \vdots & \vdots \\ \exp(-\mathrm{i}\zeta_1^+ x_n) & \exp(-\mathrm{i}\zeta_1^- x_n) \end{bmatrix} \begin{bmatrix} A_1^+ \\ A_1^- \end{bmatrix} = \begin{bmatrix} \tilde{p}_{\mathrm{exp},1} \\ \tilde{p}_{\mathrm{exp},2} \\ \vdots \\ \tilde{p}_{\mathrm{exp},n} \end{bmatrix}, \tag{6}$$

7

where $\zeta_j^{\pm}$ is the plane wave axial wavenumber. A similar procedure is applied to the downstream section. The matching condition applied at the interfaces between the sections considers continuity of mass and momentum, as proposed by Gabard and Astley [46] and described by Spillere et al. [14].

The MM algorithm requires as input an initial guess for the liner impedance together with the amplitudes of the plane waves traveling towards the sample, namely A_1^+ and A_3^-. The Levenberg–Marquadt algorithm [47, 48] is then used to minimize the cost function

$$\mathcal{F}(\tilde{Z}, \omega) = \sum_{i=1}^{n} \left| \frac{\tilde{p}_{\text{exp},i}(\omega) - \tilde{p}_{\text{MM},i}(\tilde{Z}, \omega)}{\tilde{p}_{\text{exp},i}(\omega)} \right|, \tag{7}$$

where $\tilde{p}_{\text{exp},i}$ and $\tilde{p}_{\text{MM},i}$ are the measured and theoretical acoustic pressure, respectively, at each microphone. Once convergence criteria is achieved, the liner's impedance is educed.

The MM method experimental results are obtained using two sets of $n = 4$ microphones, whose streamwise coordinates are listed in Table 1. These microphones are flush-mounted on the opposite wall of the liner sample at $z = W$. In contrast, the numerical simulations involve two arrays of $n = 22$ pressure probes located along the centerline of the channel at $y = -H$ and $z = W_p/2$, to minimize turbulence noise in the signal. The probes are evenly spaced in the streamwise direction and are situated at $W_p \le |x| \le W_p + 2L$, with a spacing of 1/2 inch between each probe.

Table 1   Streamwise coordinate of the microphones used for the experimental MM method impedance eduction.

	Mic. 1	Mic. 2	Mic. 3	Mic. 4	Mic. 5	Mic. 6	Mic. 7	Mic. 8
x Coordinate, m	-0.48	-0.31	-0.22	-0.17	0.59	0.64	0.73	0.90

C. The Prony-like Kumaresan-Tufts Algorithm

The application of the Prony-like Kumaresan-Tufts (KT) algorithm to educe the liner's impedance relies on the acoustic pressure measurement on equally spaced microphones located in the lined section, namely section $j = 2$ represented in Fig. 9. More details can be found in Watson et al. [28] and Bonomo et al. [15].

The solution of the acoustic field in the lined section is given by a sum of downstream and upstream propagating modes [15]. Considering the Ingard-Myers BC for the lined wall and $\partial \tilde{p}/\partial y = 0$ on the opposite rigid wall, one may find the eigenvalue problem

$$\alpha_m \tan\left(\alpha_m 2H\right) - \frac{Z_0}{ik\tilde{Z}}\left(ik - i\overline{M}\zeta_m\right)^2 = 0, \tag{8}$$

where α_m is the m-th transverse wavenumber and $\overline{M}$ is the grazing flow mean Mach number. The axial wavenumbers $\zeta_m^{\pm}$ are obtained by considering that the acoustic field at the lined section is a linear combination of damped complex exponentials truncated at a maximum mode number $\mathcal{N}$, giving

$$\tilde{p}_i = \sum_{m=1}^{\mathcal{N}} A_m^{\pm} e^{-i\zeta_m^{\pm}\Delta_x} + \mathcal{W}_i, \quad i = 0, 1, ..., \mathcal{M} - 1, \tag{9}$$

where $\tilde{p}_i$ is the pressure at the i-th microphone, Δ_x is the distance between two consecutive microphones, $\mathcal{W}$ is the measurement noise and $\mathcal{M}$ is the total number of microphones. With Eq. 8 and the dispersion relation given by

$$\alpha_m^2 = \left(k - \overline{M}\zeta_m\right)^2 - \zeta_m^2, \tag{10}$$

it is straightforward to obtain the liner's impedance. For the solution of this problem, the order of the model needs to be reduced to $\mathcal{L}$, such that $\mathcal{N} \le \mathcal{L} \le \mathcal{M} - \mathcal{N}$ [15].

The KT algorithm experimental results are obtained from eight equally spaced microphones, whose streamwise coordinates are given in Table 2. These microphones are flush-mounted on the opposite wall of the liner sample, at $z = W$. Numerically, ten pressure probes are used to acquire the time signals in the lined section. Likewise the MM method probes, they are located in the center line of the channel, so as to avoid turbulence noise in the signal. The probes' x coordinates are aligned with the partition walls of the liner sample, i.e., $x_i = iW_p$, for $i = 1, 2, ..., 10$.

8
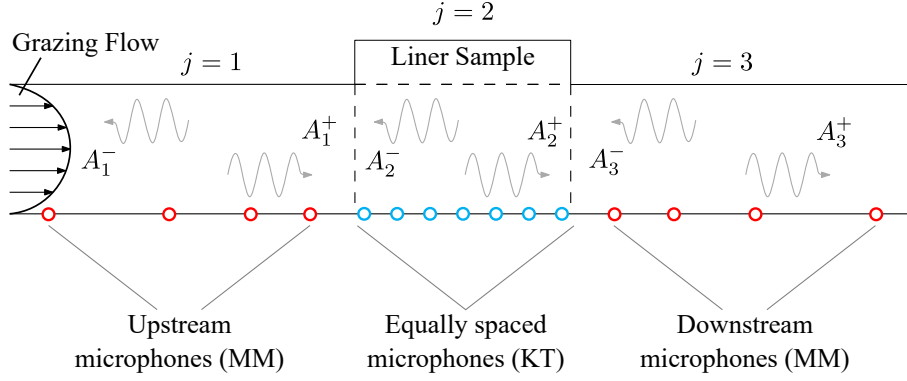
Fig. 9 Impedance eduction techniques schematic: theoretical acoustic field and microphones' positions.

Table 2 Streamwise coordinate of the microphones used for the experimental impedance eduction with the KT algorithm.

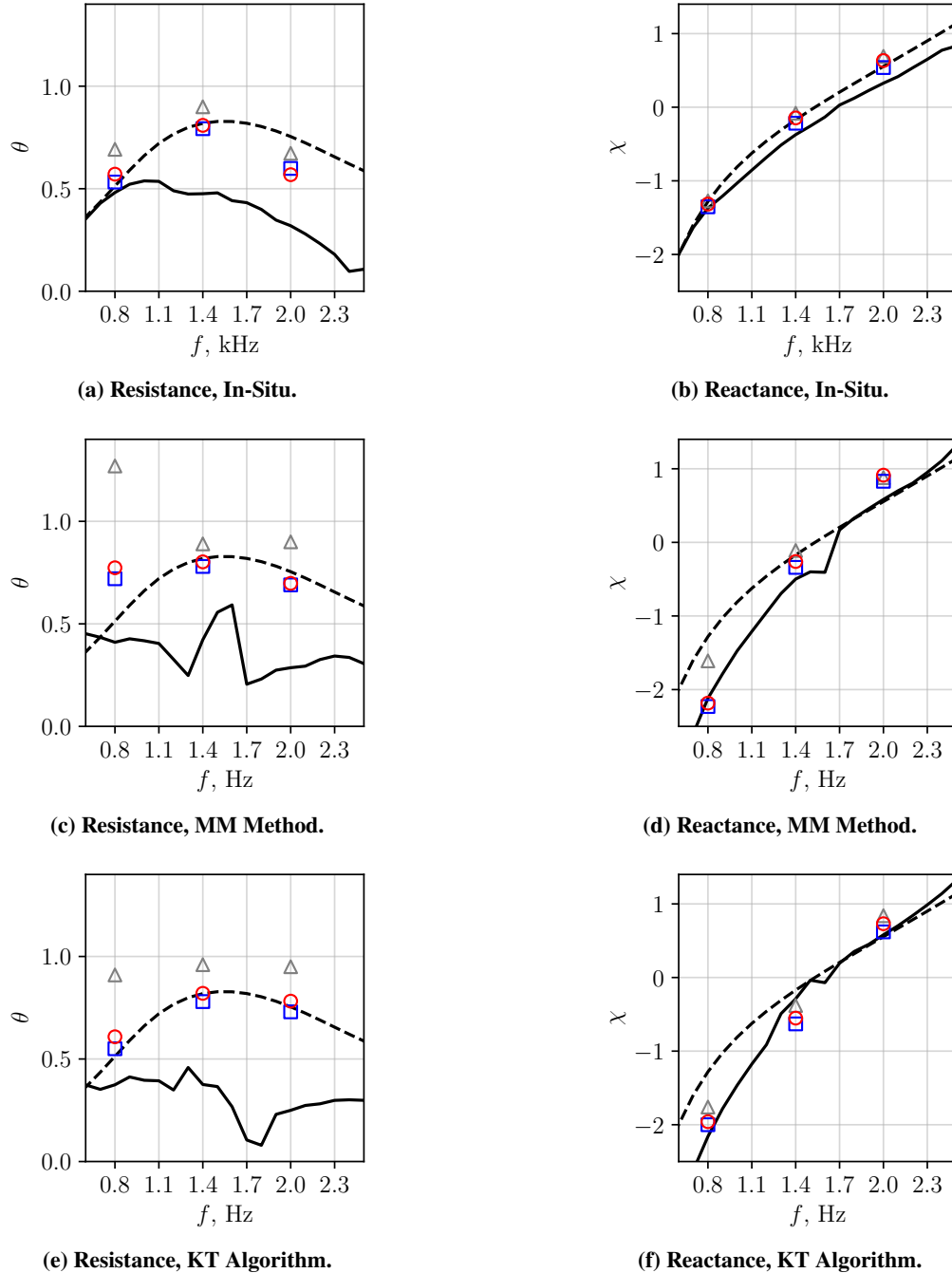|	Mic. 1	Mic. 2	Mic. 3	Mic. 4	Mic. 5	Mic. 6	Mic. 7	Mic. 8
x Coordinate, m	0.08	0.12	0.16	0.20	0.24	0.28	0.32	0.36

IV. Results

This section compares the acoustic impedance obtained from simulations at 800Hz, 1400Hz, and 2000Hz, with 145dB, with experimental measurements conducted in the UFSC test rig and the semiempirical model by Yu et al. [26]. The comparisons are made in absence and in presence of grazing flow. Firstly, the results for the liner's impedance in the absence of grazing flow are shown. Then, a comparison between the TBL measured in the UFSC test rig and the TBL developed in the simulation channel is presented for a grazing flow with centerline $M = 0.32$. This comparison is based on the three impedance measurement techniques described in Section III. Afterward, a discussion on the impedance measurements in the presence of grazing flow is carried out for acoustic sources located at both upstream and downstream positions with respect to the liner. The results are compared for the three impedance measurement techniques individually. The flow-acoustic interaction is analyzed in the near-orifice regions.

A. Acoustic Results in the Absence of Grazing Flow

Simulations were performed to evaluate the liner's impedance in the absence of grazing flow at the three grid resolutions studied, in order to determine the convergence of the results. Inadequate grid resolutions can result in an inaccurate solution for the flow inside the liner's orifices, which is a potential cause for misleading the impedance measurements. Fig. 10 presents the simulation results obtained in comparison with the experimental measurements and with the semiempirical model predictions. The simulation results show that there is a trend towards both smaller resistance and reactance values with increasing resolution, which agrees with previous observations reported in the literature [24, 49]. However, it is observed that the resistance is more sensitive to the grid resolution level. The simulations provide reasonable results for the impedance with all the three measurement techniques for the medium resolution level, and minor changes are verified between medium and fine resolution results. The results for the coarse resolution, on the other hand, neither agree with the experimental results nor with the model's prediction, showing that a minimum of 20 cells per orifice diameter should be used for a proper characterization of the liner in the absence of grazing flow, as a thumb rule. Moreover, the accuracy of the eduction methods' predictions are more affected by poor resolution levels, which mislead especially the low frequency resistance measurements.

The in-situ technique results are the less sensitive among the methods to the change in the grid resolution. Still the effect of the grid resolution is noticeable, especially in the resistance results. Considering the results from the fine resolution simulations, there is consistency with the semiempirical model predictions. The resistance and reactance measured with the in-situ technique are shown in Figs. 10a and 10b, respectively. The simulation result for 800 Hz agree reasonably well with the experiments and the model. As the frequency increases, the experimental curve and the model's predictions deviate from each other, the latter overestimating the former. However, the trends of both the

(a) Resistance, In-Situ.

(b) Reactance, In-Situ.

(c) Resistance, MM Method.

(d) Reactance, MM Method.

(e) Resistance, KT Algorithm.

(f) Reactance, KT Algorithm.

Fig. 10 Comparison of the liner's impedance obtained from the simulations for $M = 0$ cases with the acoustic source set to 145 dB: experimental (—); semiempirical model (- -); simulations, coarse ($\triangle$); simulations, medium ($\bigcirc$); simulations, fine ($\square$).

model and the experiments are very similar, which might be related to the fact that the model was built upon in-situ measurements. The results of the simulations fall in between the two baselines, and there is better agreement with the semiempirical model. The reactance values match well with the model's predictions, and present a small deviation from the experimental curve as the frequency increases. Nonetheless, the trends are well represented by the simulations, and the results are within a fair agreement with the reference values.

Figs. 10c and 10d present the MM method results. These results exhibit a significant discrepancy between the

experimental measurements and the semiempirical model predictions, particularly in the resistance plots. The generally constant trend exhibited by the MM method experimental results is not captured by the model, which can be justified by the fact that the model was built upon in-situ measurements. For the reactance, there is also a considerable deviation between the model and experimental results, especially at frequencies below resonance. The simulation results obtained with the MM method are the most sensitive to poor resolution levels, as evident from the significant changes in measured impedance with increasing resolution, particularly for the 800Hz case where both resistance and reactance values decrease towards the reference curves. With respect only to the fine resolution results, the simulations show a rather constant trend for the resistance over all the frequencies considered, but overestimate the experimental results. There is reasonable agreement with the semiempirical predictions for 1400 Hz and 2000 Hz, which is likely related to the bump presented by the model in the near resonance frequencies. Regarding the reactance, overall the simulations generally follow the experimental trend, except for a slight overprediction for the 2000 Hz case.

Figs. 10e and 10f display the results obtained from the simulations using the KT algorithm. Similar to the MM method, the model and experimental results do not exhibit the same trends, particularly for the resistance plots. In this case, the model still overpredicts the experimental results, and so do the simulations. As with the MM method, the sensitivity to the discretization level is significant. However, an increase in resolution to 40 cells/d results in a close match between the simulation results and the semiempirical model predictions for the resistance, even in the 800 Hz case where the MM method misses. Regarding the reactance, the simulations agree better with the experimental curve, which matches reasonably the model's predictions for frequencies above resonance. For frequencies below resonance, the model overestimates the experiments, as observed also in the comparison of the MM method results, and the results from the simulations present better agreement with the experiments.

Recent works have shown that different impedance measurement techniques might deliver different results for a given liner sample, especially in the presence of grazing flow [25]. However, when liners are subjected to high SPL excitation, mismatches between different measurement methods are observed even in the absence of grazing flow [12]. The in-situ technique measures the local impedance using a single pair of microphones or probes, which may not accurately represent the entire sample. Conversely, the eduction methods provide a global assessment of the liner's impact on the acoustic field, resulting in an averaged impedance value for the sample. However, it should be noted that these global effects are the combined result of the local effects measured by the in-situ technique, which is of particular interest. It is expected a change in the measured impedance in the streamwise direction of the liners, due to the SPL attenuation provided by consecutive cavities [39, 50], which can be assessed by the in-situ technique. To evaluate how the SPL, resistance and reactance change along the sample, measurements were made along the whole face sheet of the liner in the simulations. Fig. 11a shows 2D visualizations of the SPL on the liner face sheet for the 1400 Hz case. It is noticeable that the liner yields considerable attenuation, which results in a change in the measured resistance, presented by Fig. 11b. Generally, as the SPL drops, so does the resistance, for all the frequencies analyzed. On the other hand, the overall behavior of the reactance is to increase towards the last cavities of the liner, as exhibited by Fig. 11c.

Although the contour plots provide an overview of how these parameters change along the face sheet of the liner, line plots provide more detailed and quantitative information. To make these line plots, some of the probes used to make the contour plots were selected on the face sheet at a specific z coordinate. This z coordinate, shown by the red line in Fig. 12, was chosen such that none of the probes would coincide with any of the orifices. The line plots obtained from these probes are shown in Figs. 13 and 14 for the 1400 Hz and 2000 Hz cases, respectively. In these plots, the vertical white bars represent the partition walls, which separate each cavity from the adjacent ones.

From Fig. 13a, one may notice that the liner attenuates the incoming acoustic amplitude of more than 10 dB along its length for the acoustic wave with tonal frequency equal to 1400 Hz. The line plots reveal that the SPL slightly changes within the same cavity, reaching a maximum value in the near-orifice regions (center of the cavity). This reflects in the model's predictions for the resistance, exhibited in Fig. 13b, which also present a slight parabolic shape with a maximum in the near-orifice regions. These predictions agree reasonably well with the measured resistance, although the trends within each cavity are different. The resistance measured generally decay along the individual cavities, and the maximum value is not found in the near-orifice regions, but close to the left hand side partition wall. As for the reactance, the plots shown in Fig. 13c reveal that the measurements increase from the first cavity to the last one. This trend, which is not captured by the model's predictions, was also observed in previous works [24, 39]. More interestingly, perhaps, is the change in the reactance within each individual cavity. Overall, the measured values tend to drop from the partition wall on the left hand side to the right hand side. The curves of the measured reactance also exhibit a parabolic shape, but with a minimum value, which occurs in the near-orifice regions.

Fig. 14 shows the line plots for the 2000 Hz acoustic excitation. In this case, there is less attenuation provided by the liner along the eleven cavities in comparison with the 1400 Hz case, which is closer to the resonance. As a consequence,

11

(a) Sound Pressure Level.

(b) Resistance, In-Situ.

(c) Reactance, In-Situ.
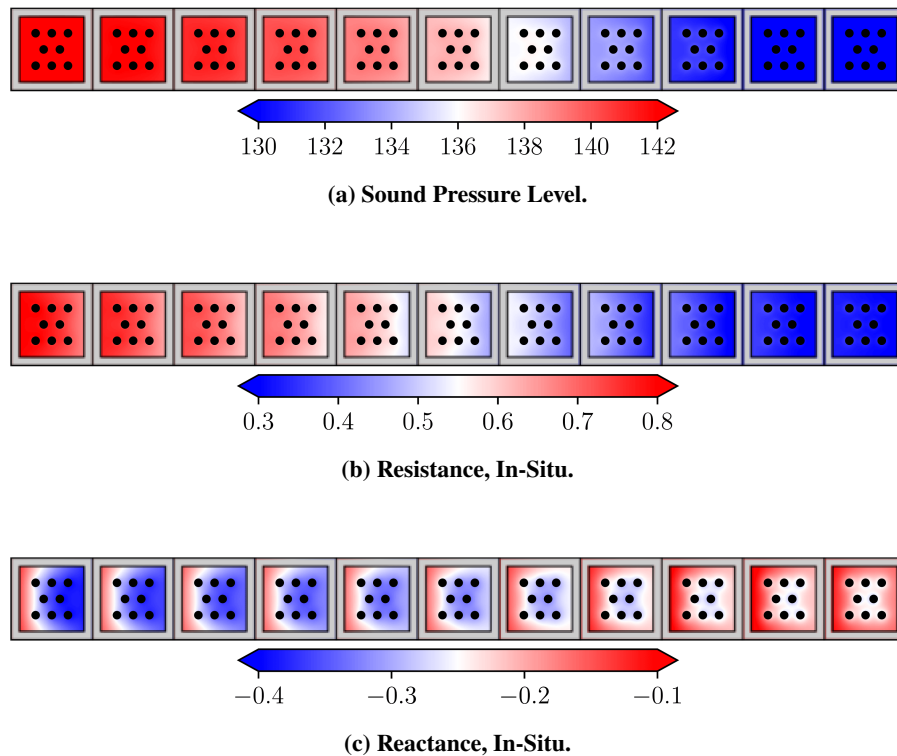
Fig. 11   Contour plots of the results obtained from the simulations (fine) on the face sheet of the liner. Case is $M = 0$ for a 1400 Hz acoustic excitation, at 145 dB. The acoustic source is positioned upstream of the sample (left hand side of the plot).
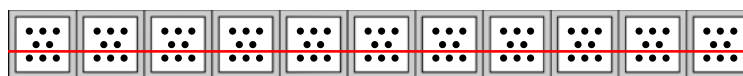
Fig. 12   Location of the face sheet probes along the sample for the line plots of sound pressure level, resistance and reactance.

a smaller variation of the mean resistance values is found along the sample. The reactance mean values, on the other hand, exhibit larger variation for the 2000 Hz case, when compared to the 1400 Hz one. The comparison between the 1400 Hz and the 2000 Hz cases shows the variation trends within each individual cavity are frequency dependent, especially for the SPL and the resistance. The assessment of the SPL for the 2000 Hz case shows a minimum value in the near-orifice regions, which is opposite to the maximum value found in the results for the 1400 Hz excitation. In contrast with a decaying resistance along each cavity, which can be observed in the 1400 Hz case, the 2000 Hz case exhibits an increasing resistance towards the right hand side partition walls. These trends are evidence that the measured impedance by the in-situ technique is a function of both the position of the face sheet probe and the streamwise position of the cavity within the sample length, even in the absence of grazing flow.

The analysis of the behavior of the resistance for the 2000 Hz case, shown in Fig. 14b, allows us to provide a possible explanation to why the semiempirical model overpredicts the resistance measured in the experiments (see Fig. 10a). Since the position of the face sheet probe in the experiments (Fig. 8a) is on the left hand side of the orifices, there is a trend for lower resistance measurements, while for frequencies below resonance the resistance values at the probe's

12

(a) Sound Pressure Level.

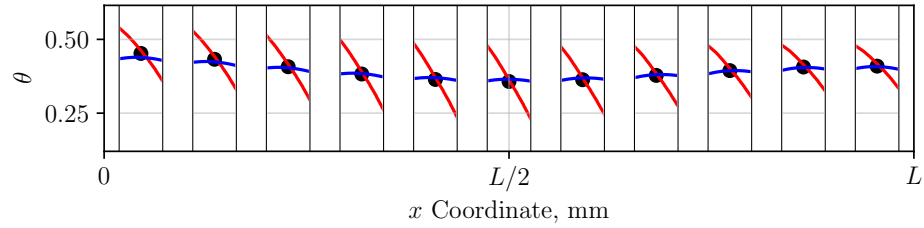**(b) Resistance, In-Situ.**

(c) Reactance, In-Situ.
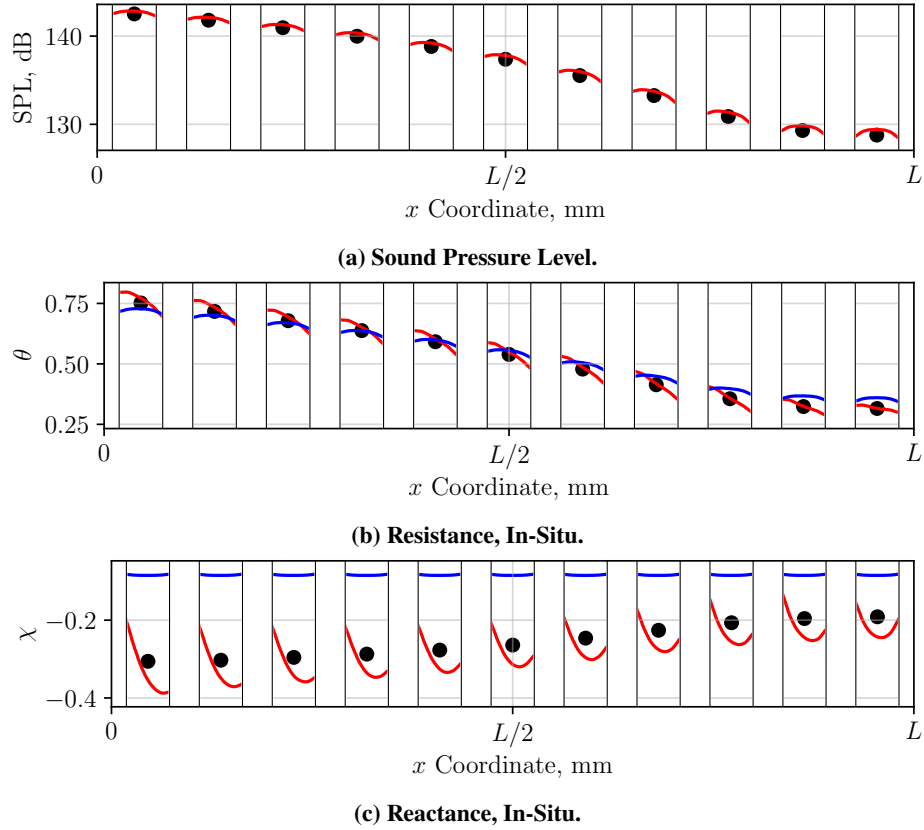
Fig. 13   Results along the liner sample obtained from the simulations (fine) on the face sheet. Case is $M = 0$ for a 1400 Hz acoustic excitation, at 145 dB. The acoustic source is positioned upstream of the sample (left hand side of the plot). Simulation data (—); mean value of the simulation data (●); semiempirical model prediction, based on the measured SPL (—).

position tend to be higher. This is supported by the analysis of the resistance behavior over the liner for the 800 Hz case, presented in Fig. 15. It is evident that the slope of the resistance is steeper, delivering higher resistance values near the probe's position.

Since we measure the impedance in the simulations at a similar position on the face sheet as the experiments, the analysis of why the model overestimates the experiments' results can be extended to the simulations. However, the difference between the latter and the model is smaller, and the most likely explanation is the difference between the SPL set to the acoustic source and the one measured at the probes. Although the source is set to 145 dB in the simulations, the measured SPL at the probe's position are 143.11 dB, 142.56 dB and 141.67 dB, respectively for the 800 Hz, 1400 Hz and 2000 Hz cases. By correcting the SPL levels in the model's predictions we get a better agreement to the simulation results, as shown in Fig. 16. Still, a small mismatch can be seen between the simulations' measurements and the predictions, which is in agreement with the variations within individual cavities discussed previously. This gives us confidence that the model is robust at this point for further analysis involving multi-cavities acoustic liners in the absence of grazing flow. In the experiments, the SPL is calibrated by plane wave decomposition with the MM method microphones, which are closer to the acoustic drivers, such that the amplitude of the mode that propagates towards the sample reaches 145 dB. For this reason, a similar phenomena can be responsible for the mismatch between the experiments and the simulations/model. In the experimental case, the SPL on the face sheet calculated by a transfer function between the reference microphone and the in-situ probe are 142.9 dB, 142.0 dB and 138.7 dB, respectively for 800 Hz, 1400 Hz and 2000 Hz. The model prediction for the corrected experimental SPL presents better agreement with the measurements, but still a considerable mismatch exists in frequencies above 1 kHz, which might be related to leakage problems due to technical issues on sealing the probe on the face sheet of the 3D printed sample, which is one of the factors related to the confidence level of the measurements carried out with the in-situ technique [13].

13

(a) Sound Pressure Level.

(b) Resistance, In-Situ.

(c) Reactance, In-Situ.
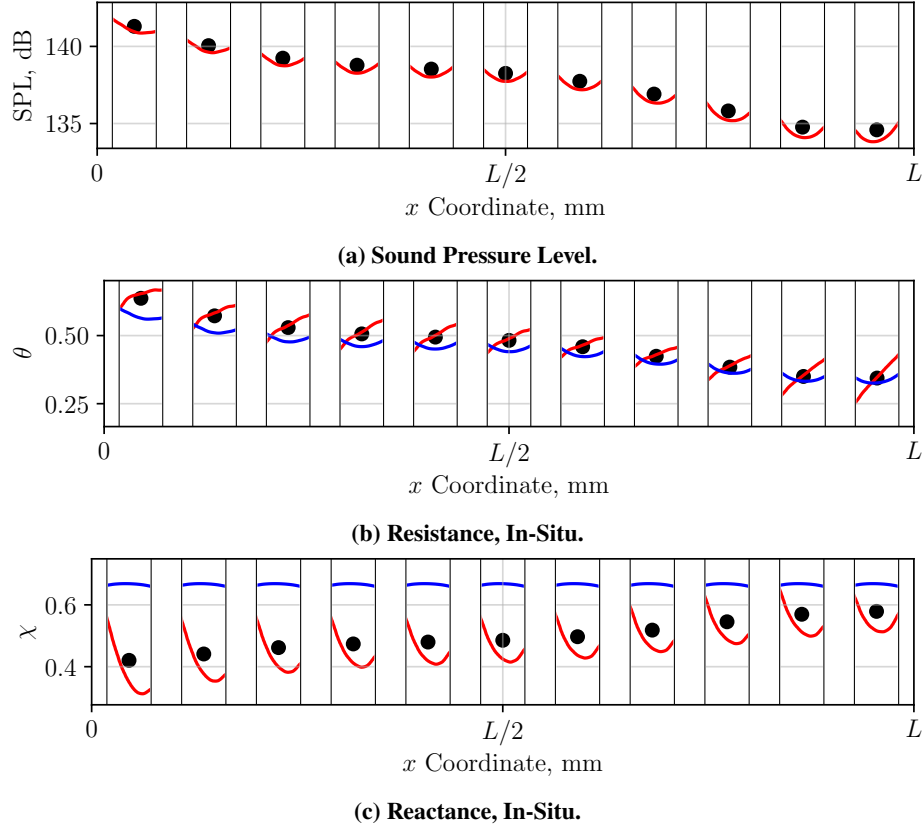
Fig. 14   Results along the liner sample obtained from the simulations (fine) on the face sheet. Case is $M = 0$ for a 2000 Hz acoustic excitation, at 145 dB. The acoustic source is positioned upstream of the sample (left hand side of the plot). Simulation data (—); mean value of the simulation data (●); semiempirical model prediction, based on the measured SPL (—).


Fig. 15   Resistance along the liner sample obtained from the simulations (fine) on the face sheet. Case is $M = 0$ for a 800 Hz acoustic excitation, at 145 dB. The acoustic source is positioned upstream of the sample (left hand side of the plot). Simulation data (—); mean value of the simulation data (●); semiempirical model prediction, based on the measured SPL (—).

B. Comparisons of the Turbulent Boundary Layer

The assessment of the TBL in the simulations used to compare with the experimental measurements is made at the upstream end of the liner, at $x = 0$ m, where the grazing flow maximum speed in the experiments is $M \approx 0.32$. In order to provide a reasonable match of the flow velocity field in the simulations with the experimental one, a $M = 0.29$ inlet velocity BC was set in the simulations. The turbulence tripping geometries, which are 0.25 mm high and 2 mm long, were positioned at $x = -1.6$ m on both top and bottom walls, together with the transition from free-slip to no-slip BCs on the walls. This way, both top and bottom TBLs are triggered to develop towards the liner sample. Fig. 17 shows the effect of the tripping geometries by switching on the VLES solver at the specified x coordinate.

14
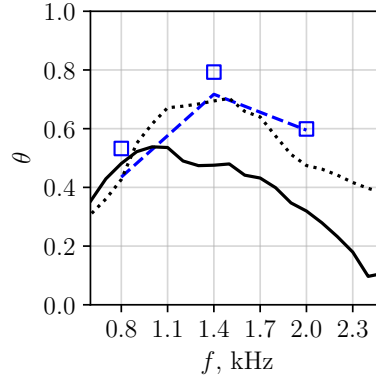
Fig. 16 Comparison of the liner's impedance obtained from the simulations for $M = 0$ cases with the acoustic source set to 145 dB: experimental (—); semiempirical model for experiments, corrected SPL (⋯); simulations, fine (□); semiempirical model for simulations, corrected SPL (- -).
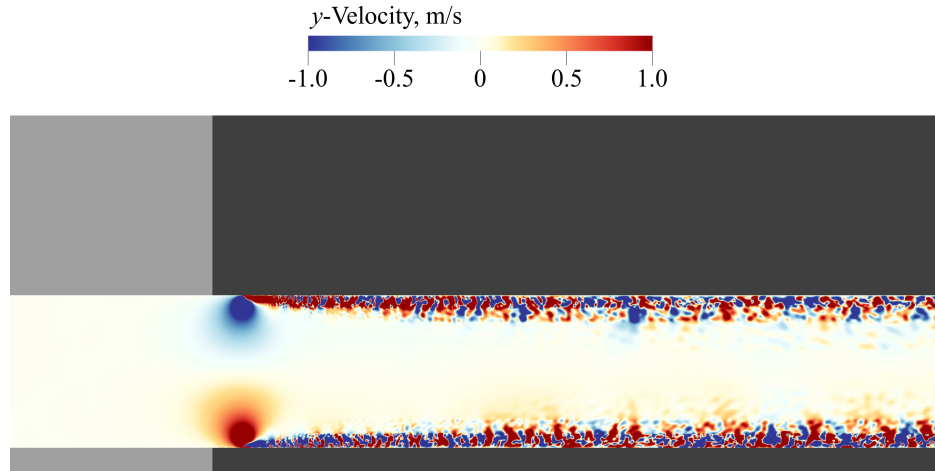

Fig. 17 Top and bottom turbulent boundary layers triggered by the tripping geometries at $x = -1.6$ m.

As the TBL develops next to both walls in the simulations, the center line flow accelerates, such that the maximum velocity at $x = 0$ is $M \approx 0.32$, likewise the experimental measurements. An overview of the comparison between the flow profiles measured in the experiments and in the simulations is shown in Fig. 18a. The experimental measurements made with the hot-wire anemometer present reasonable agreement with the Pitot tube data used as reference, and this is a good evidence that the hot-wire measurements can be trusted. The measurements from the anemometer are preferred against the Pitot tube data, since the former allows for a much more detailed assessment of the TBL, as it gets closer to the wall. It can be seen that the top and bottom TBLs from the simulations are not identical, the latter appearing less properly resolved. This is because the grid resolution next to the bottom wall is slightly less refined than the grid adjacent to the liner sample, close to the top wall. This is done to save computational resources: next to the top wall, the resolution needs to be sufficiently high to solve the flow inside the liner's orifices, where important acoustic dissipation mechanisms take place, but there is no need to such high resolution levels next to the bottom wall. Still, it is not expected that the accuracy of the model would be affected because of the slight asymmetry between the two TBLs.

Fig. 18b shows the comparison between the TBL in the experiments and the TBL assessed in the simulations, together with their respective fitting of the analytical profile, as per Schlichting and Gersten [40]. The flow profile assessed in the simulations present an overall reasonable agreement with the experimental data, even for the medium resolution case. Instantaneous measurements from the fine resolution simulations also show reasonable agreement to the experimental baseline, although this simulation has not reached statistical convergence to allow for a proper extraction of a mean profile and of the TBL parameters. For this reason, the analytical fitting of the fine resolution flow profile was omitted in Fig. 18b.

15
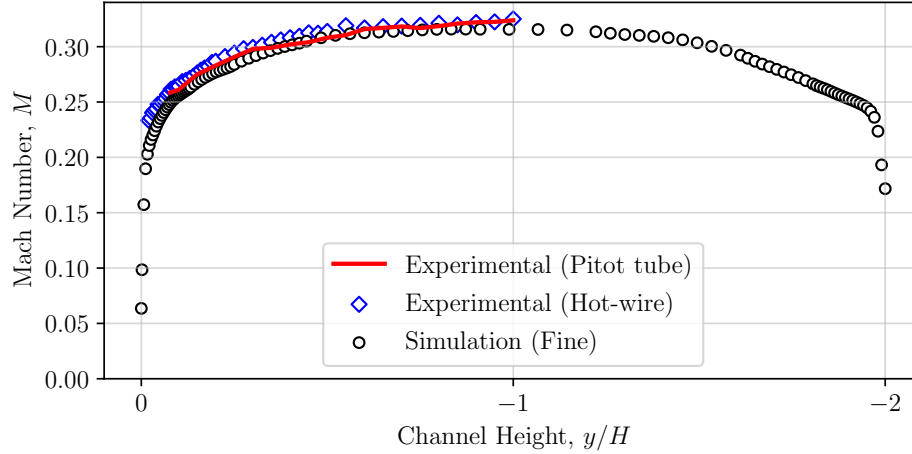
(a) Comparison of the flow profile measured experimentally by both the Pitot tube and the hot-wire anemometer with the simulations.
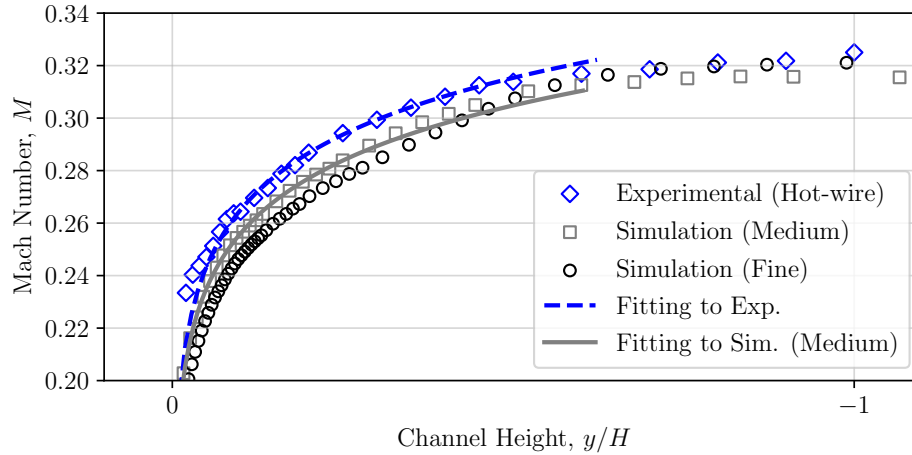
(b) Fitting of the analytical expression, as per Schlichting and Gersten [40], to the turbulent boundary layers in the experiments and in the simulations.

Fig. 18   Assessment of the flow at $x = 0$ m in both experiments and simulations.

The characterization of the TBLs in the experiments and in the simulations is made in terms of the parameters described in Table 3. The maximum Mach number M and the TBL thickness δ_{99} are obtained directly from the measured data. The mean Mach number $\overline{M}$, the TBL displacement thickness δ_1 and the TBL momentum thickness δ_2 are calculated by numerical integration. Lastly, the δ_{99} obtained from each data set are used as input parameter to the analytical fitting for the calculation of the friction velocities u_τ. This is necessary because there is not enough data close to the wall to allow for a proper estimation of u_τ, especially in the experimental measurements. To maintain consistency, the fitting is also applied to the simulations' data.

The interaction between the turbulent flow and the orifice is strongly dependent on the integral TBL parameters δ_1 and δ_2 [22]. In this work, the integral parameters normalized by the orifice diameter are $\delta_1/d \approx 1.28$ and $\delta_2/d \approx 1.11$ for the experimental flow profile, while for the simulations (medium) $\delta_1/d \approx 1.35$ and $\delta_2/d \approx 1.07$. The relative difference between the two calculated δ_1/d is about 5.5%, and for the δ_2/d there is about 3.6% difference. These relative differences are in line with previous publications from correlated experimental and numerical assessments [21], and are an improvement from the previous publication of this study [24]. As for the TBL parameters estimated for the fine resolution simulation, there is greater mismatch to the experimental reference values. However, this issue is a consequence of the lack of statistical convergence of the mean flow profile from the fine simulation, which can be addressed by extending the sampling period.

The turbulent flow induces recirculation of the flow inside the liner's orifices, which is responsible for an increase in

16

Table 3   Characteristics of the turbulent boundary layers.

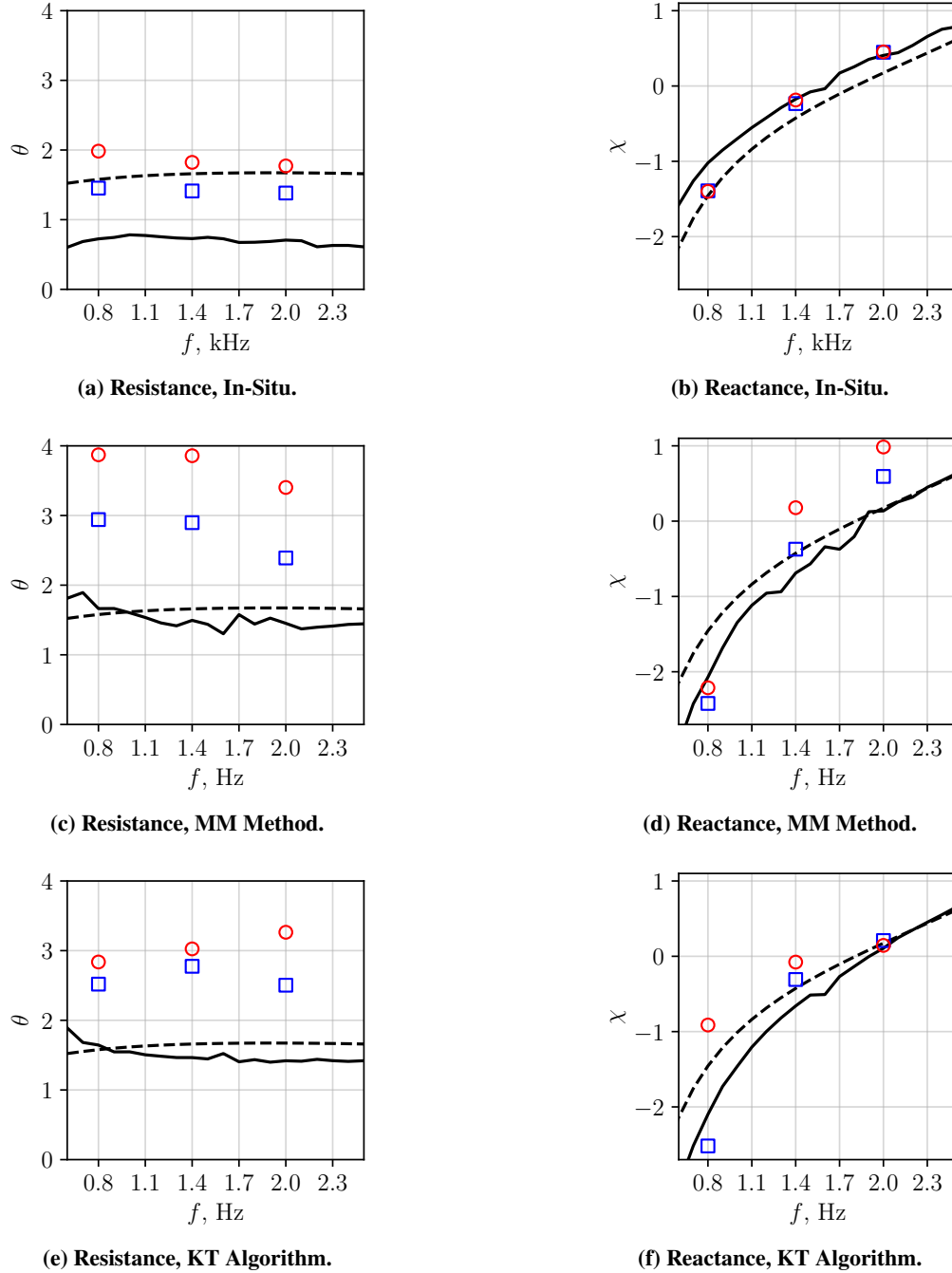|	Experimental UFSC	Simulation (Medium)	Simulation (Fine)
Maximum Mach Number M, -	0.325	0.316	0.321
Mean Mach Number $\overline{M}$, -	0.298	0.293	0.290
TBL Thickness δ_{99}, mm	12.456	12.042	13.481
TBL Displacement Thickness δ_1, mm	1.269	1.338	1.729
TBL Momentum Thickness δ_2, mm	1.099	1.060	1.342
Friction Velocity u_τ, m/s	4.420	4.300	4.171

the liner's resistance by reducing the effective area of the orifice where the oscillation induced by incident acoustic wave takes place [21, 23]. Fig. 19 shows a time-averaged result of the flow-field, where the contour plot represents the y component of the velocity. In the detail, it is possible to see the recirculation inside the orifices. Previous works have classified these recirculations as quasi-steady vortices, because they slightly oscillate within the orifice when they interact with the acoustic waves [23]. It is of primary importance to get a good representation of the fluid dynamics behaviour in this region, which include the quasi-steady vortex dimensions and its interaction with the acoustic perturbations, in order to provide a good resistance prediction.
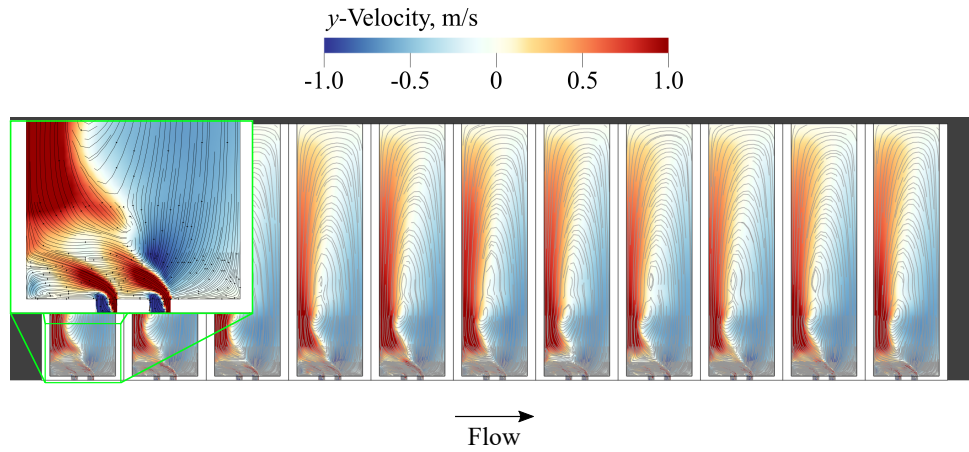
Fig. 19   Contour plot of the y velocity component of the flow, streamlines inside the cavities and detail of the near-orifice region.

C. Acoustic Results in the Presence of Grazing Flow

To analyze the convergence of the grazing flow simulations, we followed a similar approach to the $M = 0$ cases. However, since the coarse resolution grid failed to match the reference values for the $M = 0$ cases, only medium and fine resolutions were considered for the grazing flow cases. Fig. 20 presents the convergence assessment for the $M = 0.32$ simulations with an upstream acoustic source with amplitude equal to 145 dB, using the three impedance measurement methods. The simulation results were compared with the experiments and with the semiempirical model's predictions. The model's predictions showed very minor changes when using either the simulations' TBL parameters or the experimental ones as input, which suggests that the TBLs are in reasonable agreement for the acoustic analysis.

Overall, the effects of the grazing flow can be observed by the increase in the resistance values with respect to the no-flow case, exhibited by both the model and the experiments. The increase in the resistance due to the grazing flow is expected [12, 24], and it is related to the partial blockage of the orifice area by the quasi-steady vortex, shown in Fig. 19. Overall, the experimental results present a good agreement with the semiempirical model's predictions, especially for the education methods. Nonetheless, the experimental resistance results for the in-situ technique underestimate considerably the model, which are most likely related to the uncertainties of this specific technique, e.g., leakages caused

17

(a) Resistance, In-Situ.

(b) Reactance, In-Situ.

(c) Resistance, MM Method.

(d) Reactance, MM Method.

(e) Resistance, KT Algorithm.

(f) Reactance, KT Algorithm.

Fig. 20   Comparison of the liner's impedance obtained from the simulations for M = 0.32 cases with the acoustic source set to 145 dB at an upstream position: experimental (—); semiempirical model (- -); simulations, medium (○); simulations, fine (□).

by imperfect sealing of the face sheet probe and the influence of the TBL near hydrodynamic field in the measurements. As for the reactance, the eduction methods and the model are in good agreement in frequencies above resonance, while deviate from each other in lower frequencies. This was also observed for the M = 0 results, and it is most likely related to the fact that the model was adjusted to in-situ measurements, which are better represented by the model.

The assessment of the simulation results shows that there is a general trend towards smaller resistance values with increasing resolution, similar to the observations for the M = 0 cases. Once again, the eduction methods present

18

greater sensitivity to the discretization level, especially the MM method, which overpredicts considerably the reference resistances for the medium resolution cases. Considering the eduction methods, the medium resolution simulations do not provide a proper characterization of the impedance for the $M = 0.32$ cases, and even the fine resolution still overestimates the resistance by an approximate factor 2. This indicates that the computational setup needs to be improved for a proper match of the resistance with the eduction methods, either with finer resolution levels, with longer sampling times at the probes or a longer liner. Since the eduction methods rely on measurements of the acoustic field in the channel, it is important to make sure the acoustic field has reached its steady-state before sampling for the impedance. Furthermore, such a short sample in the simulations (only eleven cavities) might increase the uncertainties of the measurements. Experiments were carried out in the UFSC test rig with the same liner, but with the first and the last eleven spanwise rows of cavities covered, such that only eleven spanwise rows would interact with the flow/acoustics. The overall trends of the impedance measurements were not affected, but the curves exhibited considerable uncertainty levels in the form of spikes. The combined effects of the relative small sample length and the insufficient sampling time in the simulations are unclear, and should be further investigated.
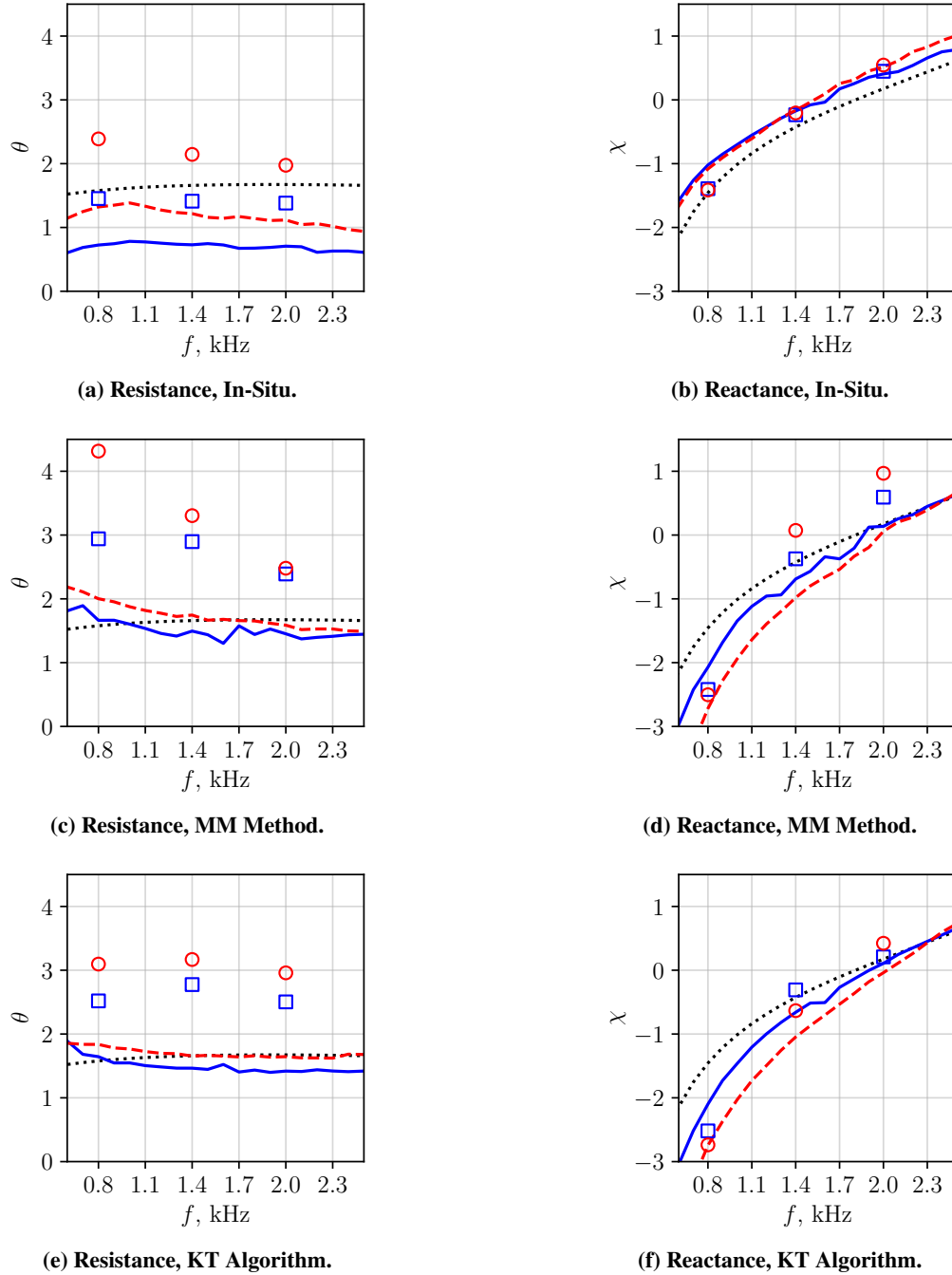
The in-situ technique result remains the less sensitive among the methods to the change in grid resolution, when there is grazing flow, and exhibits reasonable agreement with the model's predictions, for both resistance and reactance. It is expected that the in-situ measurements are less sensitive to the acoustic field in the channel, and more to the grid resolution in the orifices. This indicates the simulations are capturing the physics of the liner in the presence of grazing flow. Still, a further increase in the resolution might be necessary for a proper convergence assessment of the in-situ results, since the change from medium to fine grids brought the resistance down considerably. The results of the simulations from the eduction methods overestimate the resistance, even for the fine resolution. However, the reactance results are in reasonable agreement and the reference curves, especially with the experiments for the KT algorithm.

The effects of the position of the acoustic source in the impedance are shown in Fig. 21. All the impedance assessment methods exhibit different results for the resistance with the change in the source's position, in which the downstream source induces higher resistance than the upstream source. With respect to the eduction methods, although the downstream source experimental results are higher than the upstream ones, they are still in the range of the model's predictions. The in-situ technique exhibits the highest sensitivity to the source position, in terms of absolute values. Still, the downstream source experimental results for the in-situ remain considerably lower than the model. The change of the acoustic source position also affects reactance, but mostly for the eduction methods results. Both eduction methods exhibit a drop in reactance when the source changes from upstream to downstream, especially in the frequency range below the resonance. On the other hand, the results obtained experimentally with the in-situ technique do not exhibit significant changes with respect to the source position.

The simulations are able to capture overall the same trends observed in the experiments. The differences between upstream and downstream resistance measured in the simulations with the in-situ technique are consistent with the ones observed in the experiments, and there is very good agreement between the experiments and the simulations for the reactance results. The results obtained by the eduction methods in the simulations also change with respect to the source position. The resistances obtained from the MM method for the downstream source deviate more from the upstream results in lower frequencies, as it is the case also in the experiments. The KT algorithm, on the other hand, delivers a quite constant difference between upstream and downstream source results, both in the simulations and in the experiments. Regarding the reactance, the results from the KT algorithm in the simulations agree reasonably well with the experiments, with the downstream source values below the upstream ones, except in higher frequencies where the two curves cross and the upstream source results become higher. As for the MM method, the experimental trends from the experiments are not captured properly by the simulations, since the latter exhibit an opposite trend, i.e., the downstream source results higher than the upstream ones. This mismatch, which affects mainly the MM method, shall be further investigated.

The SPL on the face sheet for the $M = 0.32$ cases are shown in Fig. 22, for both upstream (a) and downstream (b) acoustic sources with excitation frequency equal to 1400 Hz. The streamwise distribution of SPL shows relevant differences between the two cases. When the source is located upstream, i.e. it propagates in the same direction of the mean flow, the SPL shows a minimum at the 9th and 10th cavities. The increase seen at both upstream and downstream edges of the sample is likely due to the change of surface impedance from the hard wall condition to the lined surface, and vice-versa. Similarly as for the no-flow cases, the SPL largely varies along each cell due to the presence of the partition walls between adjacent cells. When the source is located downstream, the SPL decreases almost linearly along the simulated liner sample. In this case, the edge effects are less strong than in the upstream source case. This finding suggests that the liner behaves slightly differently when changing the position of the source, and might be one explanation to the discrepancies found in the educed impedance.
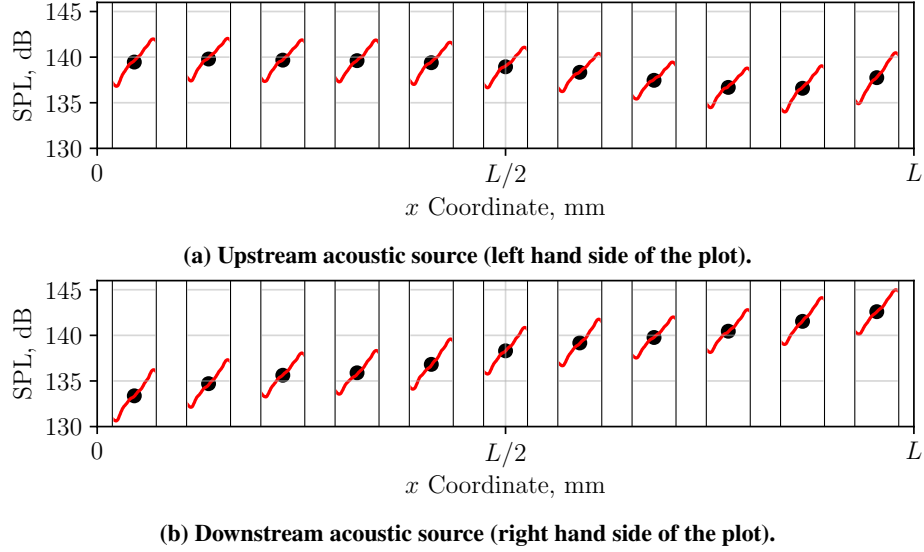
19

(a) Resistance, In-Situ.

(b) Reactance, In-Situ.

(c) Resistance, MM Method.

(d) Reactance, MM Method.

(e) Resistance, KT Algorithm.

(f) Reactance, KT Algorithm.

Fig. 21 Assessment of the liner's impedance measured in the simulations (fine) for $M = 0.32$ cases with the acoustic source set to 145 dB at both upstream and downstream positions: experimental, upstream source (—); experimental, downstream source (- -); semiempirical model (····); simulations, upstream source (□); simulations, downstream source (○).

To further dig into the differences between upstream and downstream sources, Fig. 23 and Fig. 24 show the contour plots of the resistance and reactance, respectively, obtained by applying the in-situ technique on the whole face sheet for the case with excitation frequency equal to 1400 Hz.

Differently from the no-flow case ($M = 0$), the presence of the grazing flow largely affects the surface distribution of impedance. In this case, we observe that, for both upstream and downstream source, the resistance increases from

(a) Upstream acoustic source (left hand side of the plot).

(b) Downstream acoustic source (right hand side of the plot).

Fig. 22   Sound pressure level along the liner sample obtained from the simulations (fine) on the face sheet. Case is M = 0.32 for a 1400 Hz acoustic excitation, at 145 dB. Simulation data, fine (—); mean value of the simulation data.

the most upstream to the most downstream part of each cell. The largest variation in resistance is found around each orifice with the lowest value measured upstream and the largest one downstream; from the surface distribution, it can be speculated that there is an effect of the interaction between the turbulent flow and the orifice caused by the periodic inflow and outflow motions in the orifice because of the acoustic excitation. These findings are further quantified in Fig. 25, where the line plots, extracted at the same spanwise location as for the no-flow case, are plotted for both cases. It is evident that the downstream source shows the largest variation of resistance along each cell, and also along the entire liner sample. The range of variation of the resistance within the same cell is the highest in the cavity with the lowest mean SPL (at the most left hand side), for the downstream source case. Differently, for the upstream source case the cavities with the lowest mean SPLs have the lowest variation of amplitude of the resistance.

The surface distribution of reactance, displayed in Fig. 24, shows that measurements tend to decrease towards the direction of propagation of the acoustic wave, for both upstream and downstream sources. This is further detailed in Fig. 26. The effect of the near orifice wake is also evident, as a region with lower reactance with respect to the surroundings. The streamwise distribution of mean reactance is rather uniform along the liner sample, for both upstream and downstream source. However, while for the downstream source the variation along each cell is almost the same for all the them, larger variations are found for the upstream source case.

D. Analysis of the Acoustic-Induced Velocity

To assess the effects of the mean flow on the liner behavior, the acoustic-induced velocity within the liner orifice is computed by means of a triple decomposition procedure as proposed by Avallone and Casalino [23], based on time synchronous averaging of the signals [51, 52]. The procedure consists of the following steps: a phase-average on the time signal is first performed, resulting in the phase-locked velocities, indicated as $\tilde{u}$, $\tilde{v}$ and $\tilde{w}$ for the x, y and z components, respectively; the phase-locked results are then averaged and the resulting mean velocity components are indicated as $\bar{u}$, $\bar{v}$ and $\bar{w}$; the acoustic-induced velocity is obtained by subtracting the mean velocity field from the phase-locked field, and the three acoustic-induced velocity components are indicated as $\bar{\bar{u}}$, $\bar{\bar{v}}$ and $\bar{\bar{w}}$. In this context, the acoustic-induced velocity is the zero-mean velocity fluctuation within the orifice with frequency equal to the one of the acoustic excitation.

Contours of the vertical acoustic-velocity $\bar{\bar{v}}$ component are shown in Fig. 27 for the phase corresponding to the inflow. Contours are super-imposed with the vectors obtained from the phase-locked averaging. The three sub-figures represent (a) the most upstream cell for the no-flow case, (b) the most upstream cell for the grazing flow case and upstream source, (c) the most downstream cell for the grazing flow case and downstream source. For all the cases, data
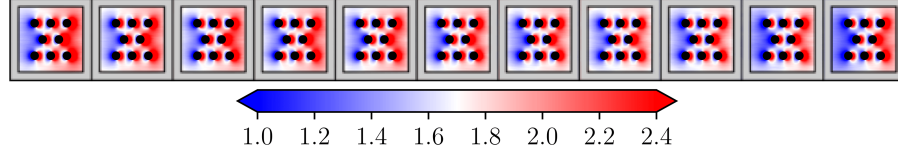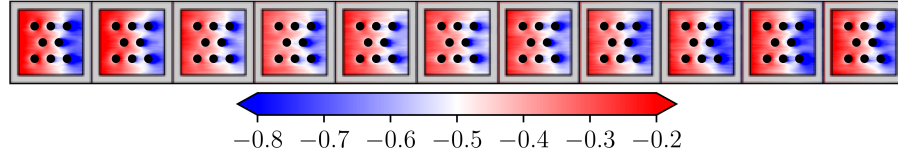
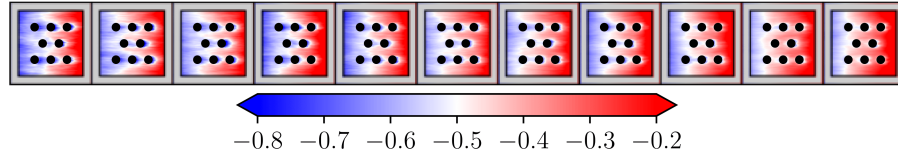**(a) Upstream acoustic source (left hand side of the plot).**
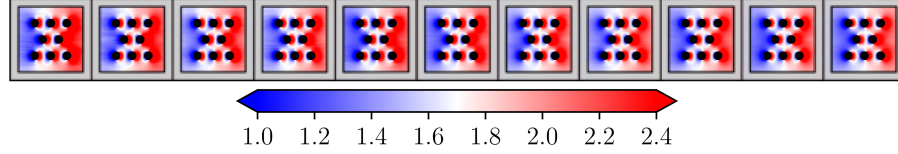
(b) Downstream acoustic source (right hand side of the plot).

Fig. 23   Contour plots of the resistance obtained from the simulations (fine) on the face sheet of the liner. Case is $M = 0.32$ for a 1400 Hz acoustic excitation, at 145 dB.

(a) Upstream acoustic source (left hand side of the plot).
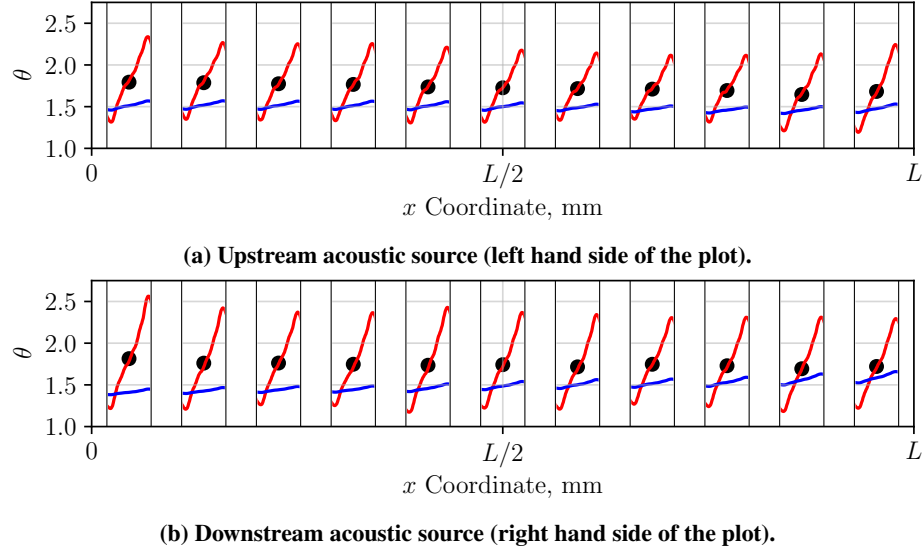

(b) Downstream acoustic source (right hand side of the plot).

Fig. 24   Contour plots of the reactance obtained from the simulations (fine) on the face sheet of the liner. Case is $M = 0.32$ for a 1400 Hz acoustic excitation, at 145 dB.
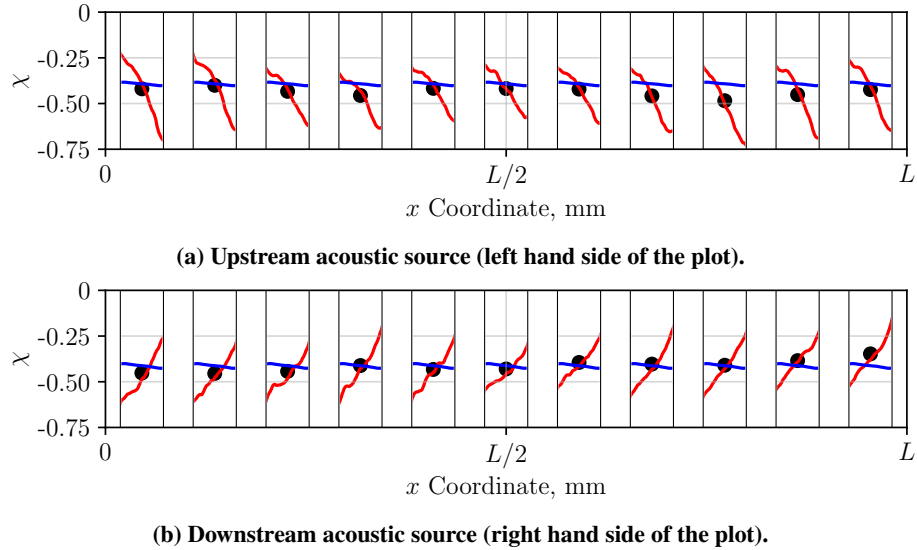
are extracted at the mid span ($z = W_p/2$).

The plots show that, in the absence of grazing flow, the flow behavior within the orifices is as reported in previous works [29, 53]. During the injection phase, the flow is directed within the cavity, and two vortices are generated and injected within the cavity as a result of the shear forces. Because of the high SPL case under investigation, the strength of the vortices is large and they can also interact, thus confirming the non-linear response of the liner [29]. The distribution of the vertical phase-locked velocity component within each orifice is symmetric, as further shown in Fig. 28, where both the inflow and outflow phase are reported.

Conversely, when there is grazing flow over the sample, the quasi-steady vortex is present and it alters the effective porosity of the liner. As show in Fig. 27, only the most downstream region of each orifice, with respect to the mean flow direction, is characterized by the largest amplitude of the acoustic-induced velocity. This is because, in this region, the effect of the vortex is negligible.

(a) Upstream acoustic source (left hand side of the plot).

(b) Downstream acoustic source (right hand side of the plot).

Fig. 25   Resistance along the liner sample obtained from the simulations (fine) on the face sheet by the in-situ technique. Case is $M = 0.32$ for a 1400 Hz acoustic excitation, at 145 dB. Simulation data, fine (—); mean value of the simulation data, fine (●); semiempirical model prediction, based on the measured SPL (—).

(a) Upstream acoustic source (left hand side of the plot).

(b) Downstream acoustic source (right hand side of the plot).

Fig. 26   Reactance along the liner sample obtained from the simulations (fine) on the face sheet by the in-situ technique. Case is $M = 0.32$ for a 1400 Hz acoustic excitation, at 145 dB. Simulation data, fine (—); mean value of the simulation data, fine (●); semiempirical model prediction, based on the measured SPL (—).

The acoustic-induced velocity and the phase-locked velocity are further compared in Fig. 28. As reported in previous studies [23], the acoustic-induced velocity shows a symmetric behavior between inflow and outflow cycles that is not present in the phase-locked results. Comparing downstream and upstream sources with the no-flow case, it is visible that the maximum acoustic induced-velocity is very similar, but the downstream source case shows higher velocity in the downstream edge of the orifice with respect to the upstream source case. This intuitively translates in a slightly larger resistance for the upstream source case with respect to the downstream one, which is similar to what is shown in Fig. 25 at these specific cavities. As it can be seen in Fig. 22, there is lower SPL in the first cavity for upstream source when comparing with the last cavity for downstream source, which might be the cause for the higher $\bar{\bar{v}}$ values found for the latter case. Although higher SPL typically translates into higher resistance, at least for the no-flow cases, this might

23

(a) $M = 0$**, first cavity.**

(b) $M = 0.32$**, upstream source, first cavity.**

(c) $M = 0.32$**, downstream source, last cavity.**
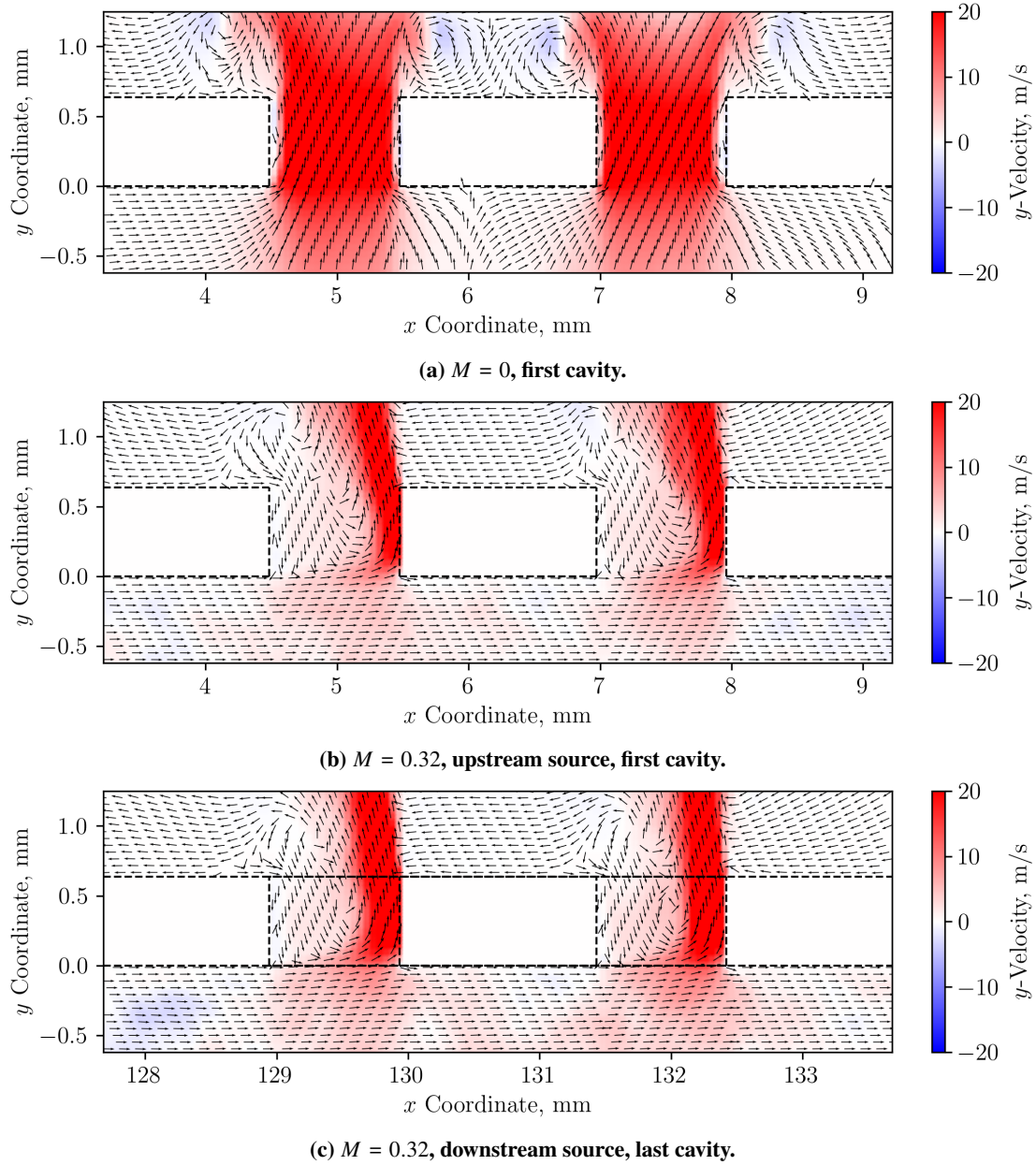
Fig. 27   Flow velocity in the orifices of the first cavity for a 1400 Hz acoustic excitation, at 145 dB, during the inflow cycle. The normalized vectors represent the direction of the phase-locked velocity field and the contour plot represents the y **component of the acoustic-induced velocity** $\bar{\bar{v}}$**.**

not be the case when there is grazing flow, since the flow non-linearities dominate. With grazing flow over the liner, the key parameter for the resistance results seems to be the effective area where the acoustic-induced oscillation takes place, which is related to the quasi-steady vortices. Further investigations are required in this matter.

V. Conclusions

This paper presented acoustic impedance results for a reference SDOF liner geometry obtained with high-fidelity numerical simulations. The impedance was measured by the in-situ technique and by two eduction methods (the mode matching method and the KT algorithm), which were compared to experimental results obtained in the UFSC test rig

24
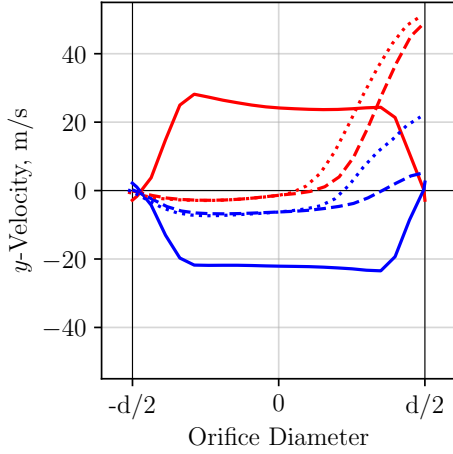
(a) Phase-locked velocity $\tilde{v}$, y component.
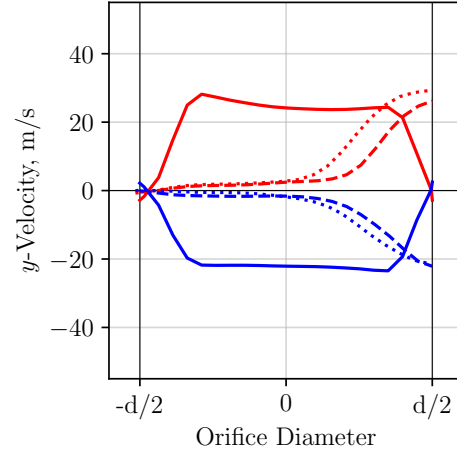
(b) Acoustic-induced velocity $\bar{\bar{v}}$, y component.

Fig. 28   In-orifice velocity profiles from the maximum and minimum value phases, induced by a 1400 Hz acoustic excitation at 145 dB. Inflow cycles are in red, outflow cycles are in blue. First cavity, upstream source for $M = 0$ case (—); first cavity, upstream source for $M = 0.32$ case (- -); last cavity, downstream source for $M = 0.32$ case (····).

and to the semiempirical Goodrich model. Acoustic simulations for three different frequencies with amplitude equal to 145 dB were conducted for no-flow cases and for grazing flow cases of maximum Mach number equal to 0.32, with both upstream and downstream acoustic sources. The simulations presented reasonable agreement with the baselines for the no-flow cases for all the impedance measurement methods, for a mesh with at least 20 cells per orifice diameter. Impedance results for the whole face sheet showed considerable variations along the liner, and even inside a single cavity, suggesting that the in-situ measurements from a single probe might not represent the overall behavior of the sample.

The comparison between the turbulent boundary layers measured experimentally and in the simulations showed good agreement. Still, large discrepancies were observed between the acoustic results from the simulations and the experiments for the cases with flow, even for the fine resolution mesh considered in this work (40 cells per orifice diameter). Specifically, the resistance values are overestimated by the simulations at this grid resolution. The convergence study suggests that further refinements on the mesh might improve the agreement between the simulations' acoustic results and the experiments', and from previous literature it is expected that a finer resolution equal to 60 cells per diameter is the minimum to achieve converged results. The model seems sensitive enough to capture different impedance measurements when the acoustic source changes from upstream to downstream with all the methods considered. However, the mode matching method in the simulations struggles to match the experimental trends for the reactance. A reasonable hypothesis for this is that either a longer sampling time in the simulations or a longer liner sample might improve the agreement for the education methods. The analysis of the impedance along the face sheet of the sample when there is grazing flow reveals a large influence of the near-orifice wake on the results, and that in these cases the non-linearity induced by the flow dominates over the high SPL. These results are evidence of the issues regarding assessment of the impedance of liners with the in-situ technique, at least for the sampling time used in the simulations in this work.

The acoustic-induced velocity in the near-orifice regions was assessed by means of a triple decomposition approach of the velocity field. Results show that the effective area of the orifice in which the acoustic excitation is able to induce the flow oscillation is drastically reduced when there is grazing flow over the sample. This happens because the grazing flow generates a quasi-steady vortex inside the orifices that blocks its most upstream region. A slight difference in the acoustic-induced velocity profile between upstream and downstream sources was observed, but it was attributed to a difference in the sound pressure level of the excitation. Further investigations are required in this matter.

Acknowledgments

References

[1] Bertsch, L., Snellen, M., Enghardt, L., and Hillenherms, C., "Aircraft noise generation and assessment: executive summary," *CEAS Aeronautical Journal*, Vol. 10, 2019, pp. 3–9. https://doi.org/10.1007/s13272-019-00384-3.

[2] Casalino, D., Diozzi, F., Sannino, R., and Paonessa, A., "Aircraft noise reduction technologies: A bibliographic review," *Aerospace Science and Technology*, Vol. 12, 2008, pp. 1–17. https://doi.org/10.1016/J.AST.2007.10.004.

[3] Bake, F., and Knobloch, K., "Novel liner concepts," *CEAS Aeronautical Journal*, Vol. 10, 2019, pp. 123–136. https://doi.org/10.1007/s13272-019-00380-7.

[4] Murray, P., and Giulio, M. D., "Development and validation of a single degree of freedom perforate impedance model under high SPL and grazing flow," *28th AIAA/CEAS Aeroacoustics 2022 Conference*, 2022. https://doi.org/10.2514/6.2022-2929.

[5] Jones, M. G., Tracy, M. B., Watson, W. R., and Parrott, T. L., "Effects of liner geometry on acoustic impedance," *8th AIAA/CEAS Aeroacoustics Conference and Exhibit*, 2002. https://doi.org/10.2514/6.2002-2446.

[6] Eversman, W., "The Effect of Mach Number on the Tuning of an Acoustic Lining in a Flow Duct," *The Journal of the Acoustical Society of America*, Vol. 48, No. 2A, 1970, pp. 425–428. https://doi.org/10.1121/1.1912148.

[7] Kooi, J., and Sarin, S., "An experimental study of the acoustic impedance of Helmholtz resonator arrays under a turbulent boundary layer," *7th Aeroacoustics Conference*, 1981. https://doi.org/10.2514/6.1981-1998.

[8] Méry, F., Piot, E., Sebbane, D., Reulet, P., Simon, F., and Méndez, A. C., "Experimental assessment of the effect of temperature gradient across an aeroacoustic liner," *Journal of Aircraft*, Vol. 56, 2019, pp. 1809–1821. https://doi.org/10.2514/1.C035157.

[9] Murray, P. B., and Astley, R. J., "Development of a single degree of freedom perforate impedance model under grazing flow and high SPL," *18th AIAA/CEAS Aeroacoustics Conference*, 2012. https://doi.org/10.2514/6.2012-2294.

[10] Jones, M. G., Watson, W. R., Parrott, T. L., and Smith, C. D., "Design and evaluation of modifications to the NASA Langley flow impedance tube," *10th AIAA/CEAS Aeroacoustics Conference*, Vol. 1, 2004, pp. 451–463. https://doi.org/10.2514/6.2004-2837.

[11] Léon, O., Méry, F., Piot, E., and Conte, C., "Near-wall aerodynamic response of an acoustic liner to harmonic excitation with grazing flow," *Experiments in Fluids*, Vol. 60, 2019. https://doi.org/10.1007/s00348-019-2791-5.

[12] Bonomo, L. A., Quintino, N. T., Spillere, A., Cordioli, J. A., and Murray, P. B., "A Comparison of In-Situ and Impedance Eduction Experimental Techniques for Acoustic Liners with Grazing Flow and High SPL," *28th AIAA/CEAS Aeroacoustics 2022 Conference*, 2022. https://doi.org/10.2514/6.2022-2998.

[13] Dean, P. D., "An in situ method of wall acoustic impedance measurement in flow ducts," *Journal of Sound and Vibration*, Vol. 34, 1974, pp. 97–IN6. https://doi.org/10.1016/S0022-460X(74)80357-3.

[14] Spillere, A. M. N., Bonomo, L. A., Cordioli, J. A., and Brambley, E. J., "Experimentally testing impedance boundary conditions for acoustic liners with flow: Beyond upstream and downstream," *Journal of Sound and Vibration*, Vol. 489, 2020. https://doi.org/10.1016/j.jsv.2020.115676.

[15] Bonomo, L. A., Spillere, A. M. N., and Cordioli, J. A., "Parametric Uncertainty Analysis for Impedance Eduction Based on Prony's Method," *AIAA Journal*, Vol. 58, No. 8, 2020, pp. 3625–3638. https://doi.org/10.2514/1.J059071.

[16] Ingard, U., "Influence of Fluid Motion Past a Plane Boundary on Sound Reflection, Absorption, and Transmission," *The Journal of the Acoustical Society of America*, Vol. 31, 1959, pp. 1035–1036. https://doi.org/10.1121/1.1907805.

[17] Myers, M., "On the acoustic boundary condition in the presence of flow," *Journal of Sound and Vibration*, Vol. 71, No. 3, 1980, pp. 429–434. https://doi.org/10.1016/0022-460X(80)90424-1.

[18] Renou, Y., and Aurégan, Y., "Failure of the Ingard–Myers boundary condition for a lined duct: An experimental investigation," *The Journal of the Acoustical Society of America*, Vol. 130, 2011, pp. 52–60. https://doi.org/10.1121/1.3586789.

[19] Dai, X., and Aurégan, Y., "Acoustic of a perforated liner with grazing flow: Floquet-Bloch periodical approach versus impedance continuous approach," *The Journal of the Acoustical Society of America*, Vol. 140, 2016, p. 2047. https://doi.org/10.1121/1.4962490.

[20] Boden, H., Cordioli, J. A., Spillere, A., and Serrano, P., "Comparison of the effect of flow direction on liner impedance using different measurement methods," *23rd AIAA/CEAS Aeroacoustics Conference*, 2017. https://doi.org/10.2514/6.2017-3184.

[21] Zhang, Q., and Bodony, D. J., "Numerical investigation of a honeycomb liner grazed by laminar and turbulent boundary layers," *Journal of Fluid Mechanics*, Vol. 792, 2016, pp. 936–980. https://doi.org/10.1017/jfm.2016.79.

[22] Avallone, F., Manjunath, P., Ragni, D., and Casalino, D., "Lattice-boltzmann very large eddy simulation of a multi-orifice acoustic liner with turbulent grazing flow," *25th AIAA/CEAS Aeroacoustics Conference*, 2019. https://doi.org/10.2514/6.2019-2542.

[23] Avallone, F., and Casalino, D., "Acoustic-induced velocity in a multi-orifice acoustic liner grazed by a turbulent boundary layer," *AIAA Aviation Forum*, 2021. https://doi.org/10.2514/6.2021-2169.

[24] Pereira, L. M., Bonomo, L. A., da Silva, A. R., Cordioli, J. A., and Avallone, F., "Lattice-Boltzmann Numerical Investigation of a Realistic Multi-Cavity Acoustic Liner with Grazing Flow Interactions," *28th AIAA/CEAS Aeroacoustics Conference*, 2022. https://doi.org/10.2514/6.2022-2967.

[25] Bonomo, L. A., Quintino, N. T., Cordioli, J. A., Avallone, F., Jones, M. G., Howerton, B. M., and Nark, D. M., "A Comparison of Impedance Eduction Test Rigs with Different Flow Profiles," *AIAA Aviation Forum*, 2023.

[26] Yu, J., Ruiz, M., and Kwan, H. W., "Validation of Goodrich perforate liner impedance model using NASA langley test data," *14th AIAA/CEAS Aeroacoustics Conference*, 2008. https://doi.org/10.2514/6.2008-2930.

[27] Elnady, T., Bodén, H., and Elhadidi, B., "Validation of an Inverse Semi-Analytical Technique to Educe Liner Impedance," *AIAA Journal*, Vol. 47, No. 12, 2009, pp. 2836–2844. https://doi.org/10.2514/1.41647.

[28] Watson, W. R., Carpenter, M. H., and Jones, M. G., "Performance of Kumaresan and Tufts Algorithm in Liner Impedance Eduction with Flow," *AIAA Journal*, Vol. 53, 2015, pp. 1091–1102. https://doi.org/10.2514/1.J053705.

[29] Manjunath, P., Avallone, F., Casalino, D., Ragni, D., and Snellen, M., "Characterization of Liners using a Lattice-Boltzmann Solver," *2018 AIAA/CEAS Aeroacoustics Conference*, 2018. https://doi.org/10.2514/6.2018-4192.

[30] Casalino, D., Hazir, A., and Mann, A., "Turbofan broadband noise prediction using the lattice boltzmann method," *AIAA Journal*, Vol. 56, 2018, pp. 609–628. https://doi.org/10.2514/1.J055674.

[31] Bauerheim, M., and Joly, L., "Les of the aero-acoustic coupling in acoustic liners containing multiple cavities," *AIAA Aviation Forum*, 2020. https://doi.org/10.2514/6.2020-2571.

[32] Krüger, T., Kusumaatmaja, H., Kuzmin, A., Shardt, O., Silva, G., and Viggen, E. M., *The Lattice Boltzmann Method*, Springer International Publishing, 2017. https://doi.org/10.1007/978-3-319-44649-3.

[33] Succi, S., *The Lattice Boltzmann Equation for Fluid Dynamics and Beyond*, 1st ed., Clarendon Press, 2001.

[34] Shan, X., Yuan, X. F., and Chen, H., "Kinetic theory representation of hydrodynamics: a way beyond the Navier–Stokes equation," *Journal of Fluid Mechanics*, Vol. 550, 2006, pp. 413–441. https://doi.org/10.1017/S0022112005008153.

[35] *PowerFLOW 2022 User's Guide*, Dassault Systèmes, 2022.

[36] Habibi, K., Gong, H., Najafiyazdi, A., and Mongeau, L. G., "Prediction of the Sound radiated from Low-Mach Internal Mixing Nozzles with Forced Mixers using the Lattice Boltzmann Method," *19th AIAA/CEAS Aeroacoustics Conference*, 2013. https://doi.org/10.2514/6.2013-2143.

[37] Fares, E., "Unsteady flow simulation of the Ahmed reference body using a lattice Boltzmann approach," *Computers and Fluids*, Vol. 35, 2006, pp. 940–950. https://doi.org/10.1016/j.compfluid.2005.04.011.

[38] Teixeira, C. M., "Incorporating Turbulence Models into the Lattice-Boltzmann Method," *International Journal of Modern Physics C*, Vol. 09, No. 08, 1998, pp. 1159–1175. https://doi.org/10.1142/S0129183198001060.

[39] Schroeder, L., Spillere, A. M., Bonomo, L. A., da Silva, A. R., Avallone, F., and Cordioli, J. A., "Numerical Investigation of Acoustic Liners Experimental Techniques using a Lattice-Boltzmann Solver," *AIAA Aviation Forum*, 2021. https://doi.org/10.2514/6.2021-2144.

[40] Schlichting, H., and Gersten, K., "Internal Flows," *Boundary-Layer Theory*, Springer Berlin Heidelberg, Berlin, Heidelberg, 2017, pp. 519–556.

[41] Kundu, P. K., Cohen, I. M., and Dowling, D. R., *Fluid Mechanics*, 6th ed., Academic Press, 2015.

[42] Elnady, T., and Bodén, H., "An Inverse Analytical Method for Extracting Liner Impedance from Pressure Measurements," *10th AIAA/CEAS Aeroacoustics Conference*, 2004. https://doi.org/10.2514/6.2004-2836.

[43] Spillere, A. M., Medeiros, A. A., and Cordioli, J. A., "An improved impedance eduction technique based on impedance models and the mode matching method," *Applied Acoustics*, Vol. 129, 2018, pp. 322–334. https://doi.org/https://doi.org/10.1016/j. apacoust.2017.08.014.

[44] Zhou, L., and Bodén, H., "A systematic uncertainty analysis for liner impedance eduction technology," *Journal of Sound and Vibration*, Vol. 356, 2015, pp. 86–99. https://doi.org/https://doi.org/10.1016/j.jsv.2015.07.001.

[45] Dokumaci, E., "Sound transmission in narrow pipes with superimposed uniform mean flow and acoustic modelling of automobile catalytic converters," *Journal of Sound and Vibration*, Vol. 182, No. 5, 1995, pp. 799–808. https://doi.org/10.1006/jsvi.1995.0233.

[46] Gabard, G., and Astley, R., "A computational mode-matching approach for sound propagation in three-dimensional ducts with flow," *Journal of Sound and Vibration*, Vol. 315, No. 4, 2008, pp. 1103–1124. https://doi.org/https://doi.org/10.1016/j.jsv.2008. 02.015.

[47] Levenberg, K., "A method for the solution of certain non-linear problems in least squares," *Quarterly of Applied Mathematics*, Vol. 2, 1944, pp. 164–168. https://doi.org/10.1090/qam/10666.

[48] Marquardt, D. W., "An Algorithm for Least-Squares Estimation of Nonlinear Parameters," *Journal of the Society for Industrial and Applied Mathematics*, Vol. 11, No. 2, 1963, pp. 431–441. https://doi.org/10.1137/0111030.

[49] Mann, A., Pérot, F., Kim, M. S., and Casalino, D., "Characterization of acoustic liners absorption using a lattice-Boltzmann method," *19th AIAA/CEAS Aeroacoustics Conference*, 2013. https://doi.org/10.2514/6.2013-2271.

[50] Motsinger, R. E., and Kraft, R. E., *Aeroacoustics of Flight Vehicles: Theory and Practice*, 1991, Vol. 2: Noise Control, Chap. Design and Performance of Duct Acoustic Treatment.

[51] Hochmann, D., and Sadok, M., "Theory of synchronous averaging," *2004 IEEE Aerospace Conference Proceedings (IEEE Cat. No.04TH8720)*, Vol. 6, 2004, pp. 3636–3653 Vol.6. https://doi.org/10.1109/AERO.2004.1368181.

[52] Randall, R. B., *Vibration-based condition monitoring - industrial, automotive and aerospace applications, second edition*, 2nd ed., Wiley-Blackwell, Hoboken, NJ, 2021, Chap. 5.3.1 Time Synchronous Averaging.

[53] Tam, C. K. W., and Kurbatskii, K. A., "Microfluid Dynamics and Acoustics of Resonant Liners," *AIAA Journal*, Vol. 38, No. 8, 2000, pp. 1331–1339. https://doi.org/10.2514/2.1132.